THE INFLUENCE OF INTERNAL FRICTION ON ROTORDYNAMIC INSTABILITY

A Thesis

by

ANAND SRINIVASAN

Submitted to the Office of Graduate Studies of
Texas A&M University
in partial fulfillment of the requirements for the degree of

MASTER OF SCIENCE

May 2003

Major Subject: Mechanical Engineering

THE INFLUENCE OF INTERNAL FRICTION ON ROTORDYNAMIC INSTABILITY

A Thesis

by

ANAND SRINIVASAN

Submitted to Texas A&M University
in partial fulfillment of the requirements
for the degree of

MASTER OF SCIENCE

Approved as to style and content by:

John M. Vance (Chair of Committee)	Luis San Andrés (Member)
Maurice Rahe (Member)	John Weese (Head of Department)

May 2003

Major Subject: Mechanical Engineering

ABSTRACT

The Influence of Internal Friction on Rotordynamic Instability. (May 2003)

Anand Srinivasan, B.E., University of Madras

Chair of Advisory Committee: Dr. John M. Vance

Internal friction has been known to be a cause of whirl instability in built-up rotors since the early 1900's. This internal damping tends to make the rotor whirl at shaft speeds greater than a critical speed, the whirl speed usually being equal to the critical speed. Over the years of research, although models have been developed to explain instabilities due to internal friction, its complex and unpredictable nature has made it extremely difficult to come up with a set of equations or rules that can be used to predict instabilities accurate enough for design. This thesis suggests improved methods for predicting the effects of shrink fits on threshold speeds of instability. A supporting objective is to quantify the internal friction in the system by measurements. Experimental methods of determining the internal damping with non-rotating tests are investigated, and the results are correlated with appropriate mathematical models for the system. Rotating experiments were carried out and suggest that subsynchronous vibration in rotating machinery can have numerous sources or causes. Also, subsynchronous whirl due to internal friction is not a highly repeatable phenomenon.

DEDICATION

Amma

Appa

Engineering

ACKNOWLEDGMENTS

To Dr. John Vance for giving me an opportunity to work at the Turbomachinery Laboratory, for teaching me the basics of rotordynamics and for inspiring me to the field.

To Dr. Luis San Andrés and Dr. Maurice Rahe for agreeing to be on my committee.

To Bharathwaj for his consistent support at A&M, no matter what happened.

To Arthur Picardo, Bugra Ertas and Eddie Denk for making me understand the fundamentals of mechanical engineering.

To Avijit for helping me with XLTRC.

To Pradeep who taught me the meaning of the words Logic and Reasoning.

To my uncle Gopal, my chitti Jingla, my chitappa Krishnan, my brother Prabhu for their encouragement and valuable advice.

To every friend and acquaintance of mine who has made this possible and who has been on my side.

NOMENCLATURE

a_{cen}	=	Acceleration of the center of the shaft
a_{end}	=	Acceleration of the end of the shaft
Bd	=	Ball diameter
c_i	=	Coefficient of internal damping
c_{Modal}	=	Modal damping of the system
C_{90}	=	Damping at 90 degree phase
D	=	Axial distance
F	=	Applied force
F_s	=	Sampling rate
$F_{\tan}$	=	Tangential force due to whirling
h	=	Hysteretic damping coefficient
K	=	Stiffness of the system
$K_{eq(di)}$	=	Equivalent stiffness of the disk
$K_{eq(sh)}$	=	Equivalent stiffness of the shaft
m_d	=	Mass of the disk
m_s	=	Mass of the shaft
$M_{eq(sh)}$	=	Equivalent mass of the shaft
m_{cen}	=	Mass at the center of the shaft
m_{end}	=	Mass at the end of the shaft
M_{90}	=	Magnitude of the transfer function at 90 degree phase
$M_{eq}, K_{eq}, C_{eq}, F_{eq}$	=	Equivalent mass, stiffness, damping, force of the 1 DOF system
Pd	=	Pitch diameter
r	=	Whirl radius
T	=	Taper ratio

X_1, X_2	=	Displacements of the masses
Z_i	=	Normalized displacements
v_{cen}	=	Velocity at the center of the shaft
v_{end}	=	Velocity at the end of the shaft
b_b	=	Contact angle
d	=	Logarithmic decrement
w	=	Shaft rotative speed
w_{cr}	=	Critical speed of the system
w_d	=	Damped natural frequency of the system
$w_{n(di)}$	=	Natural frequency of the disk
$\dot{f}$	=	Whirl speed
ΔF	=	Frequency resolution
N	=	Number of samples
Δt	=	Sampling period
x	=	Damping ratio

TABLE OF CONTENTS

Page

Page

LIST OF FIGURES

Page

Page

Page

LIST OF TABLES

Page

CHAPTER I

INTRODUCTION

A recurring problem in rotordynamics is the whirl instability caused by internal friction in a built-up rotor. Though this friction dampens and suppresses the amplitude of free vibrations when the rotor is non-rotating, the friction induces self-excited vibrations at high rotor speeds and causes the amplitude of vibrations to increase until it reaches a limit cycle or until it causes destruction to the system; this is termed as rotordynamic instability.

In rotating systems, friction or damping is classified into two categories. The first category is damping in non-rotating parts, and is called external damping or external friction. Examples are bearing damping and air drag, which stabilize the system. The second category is internal friction, which acts in the rotating parts, and drives the rotor unstable at speeds above the critical speed. Though past researchers have modeled the internal friction as viscous, recent analyses and experiments show that internal friction is dominantly hysteretic rather than viscous.

The instability caused by internal friction causes the rotor to begin to whirl at shaft speeds greater than the critical speed. The whirl frequency is usually equal to a critical speed of the rotor. In most cases, the whirl instability can be suppressed with hardware fixes such as changing the bearings to softer supports with asymmetric stiffness, adding more external damping or tightening the interference fits. However, predicting the threshold speed of instability in built-up rotors at the design stage still remains a challenge, since quantifying internal friction numerically is a difficult task. Hence the need arises to develop a suitable model to predict the characteristics of built-up rotors at high speeds.

This thesis follows the style and format of the ASME Journal of Turbomachinery.

The objectives of this research are:

1. To develop an improved capability to predict the threshold speed of instability in built-up rotors with shrink and other types of interference joints.
2. To measure subsynchronous vibrations from various sources and to classify them as benign or potentially unstable, thus providing a diagnostic tool.
3. To study the effect of foundation stiffness and rotor imbalance on the onset speed of instability due to internal friction.
4. To explore experimental methods of quantifying internal friction in rotors.

CHAPTER II

LITERATURE REVIEW

The design philosophy applied to rotating machinery initially began with the construction of very stiff rotors that would ensure operation below the first critical speed. It was only after Jeffcott's [1] analysis in 1919, when he showed that rotors could be made to run beyond the first critical speed with proper rotor balancing that the trend in rotordynamics design changed. As the rigid rotor model was replaced by the more flexible one, several failures were encountered when operating at speeds above the first critical speed. Most of the failures were of unknown origin at that time. Newkirk [2] of General Electric Research Laboratory investigated the failures of compressor units in 1924, and found that these units encountered violent whirling at speeds above the first critical, with the whirling rate being equal to the first critical speed. If the rotor speed were increased above its initial whirl speed, the whirl amplitude would increase, leading to rotor failure. The speed at which the rotor begins to whirl is the onset speed of instability. Kimball [3], working with Newkirk, suggested internal friction to be the cause of shaft whirling. He showed that below the first critical speed, the internal friction would damp out the whirl motion, while above the critical speed, it would sustain the whirl.

After a series of experiments, Newkirk and Kimball arrived at a number of conclusions, the most important being: the onset speed of whirling or the whirl amplitude is unaffected by rotor balance, whirling always occurs above the first critical, whirling is encountered only in built-up rotors, increasing the foundation flexibility or increasing the damping to the foundation increases the whirl threshold speed.

In 1964, Ehrich [4] conducted an analysis of the instability induced by internal damping in a rotor and showed that the induced whirl need not necessarily excite the fundamental mode and that for various damping conditions a particular mode would be excited. He showed that in general, whirling occurs in the mode whose whirl speed is approximately one half of the rotational speed.

Gunter [5] in 1967 provided a theoretical explanation to Newkirk's findings. He modeled a flexible rotor on elastic supports and was able to come up with an analytical expression to predict the onset speed of instability. He was able to prove that rotor balance has no effect on the stability. He also proved that decreasing the foundation stiffness increased the threshold speed of whirl instability.

In 1969, Gunter and Trumpler [6] showed that in the absence of bearing damping a symmetric flexible foundation would reduce the rotor critical speed and also the whirl threshold speed. They also showed that if external damping was added, the threshold speed could be greatly improved. They also showed that foundation asymmetry without foundation damping can cause a large increase of the onset speed of instability.

Begg [7] in 1976 conducted a stability analysis due to friction induced whirl for a simple flexible rotor and showed that there exists regimes of stability, depending on the stiffness and damping characteristics. Begg computed a stability chart to determine whether a disturbance would decay, grow or remain bounded during or after removal of the disturbance.

Vance and Lee [8] in 1973 did a mathematical analysis to determine the threshold speed of instability of non-synchronous whirl for an unbalanced flexible rotor on a rigid foundation. They proved that the threshold speed is the same for balanced and unbalanced rotors. They concluded that rotors can operated safely up to speeds about eighty percent above the significant critical speed if external damping is larger than internal friction, and that shaft stiffness orthotropy has an insignificant effect on friction-induced whirl.

Black [9] in 1976 used a hysteretic model to predict that there would be a finite speed range of whirl instability, which could be passed through safely. Ying and Vance [10] verified this in 1994 by performing tests on a built-up rotor. The internal friction was found to vary with temperature and the tightness of fit. The amount of damping of the rotor on bearings could not be accurately found since the bearing stiffness varied with the angular position of the shaft.

Bently and Muszynska [11] (1985) were able to produce self excited vibrations on a shaft by covering it with a 4-mil thick layer of damping material commonly used for vibration control

(acrylic adhesive, ISD-112). They were able to prove that the damping material increased the internal friction on the shaft.

Lund [12] in 1986 studied the destabilizing forces due to internal friction using viscous, coulomb, hysteretic and micro-slip models. He compared them based on the energy input to the whirl motion, and developed conditions for instability due to internal friction in a micro-slip.

Parker [13] (1997) and Vance (1996) developed a procedure to measure the internal friction of a built-up rotor. The rotor was freely suspended and excited with a shaker. It was found that the first mode on bearings could be approximated with the free-free mode shape by adding extra masses to the ends of the rotor. The logarithmic decrement could then be found and converted to an equivalent viscous and hysteretic damping coefficient, which could be used in rotordynamic codes to predict the instability. The rule of thumb that Parker came up with for the mass to be added to the end of the rotor was that the mass should be twice the weight of the rotor. This requirement makes the procedure impractical for heavy rotors.

Bently [14] in 1972 revisited Kimball's 1924 papers and showed that internal friction produces forward whirl with circular orbits, thus driving the system unstable.

Mir and Khalid [15], [16] (2001) showed that the measure of the logarithmic decrement from free-free rap tests of the shrink fit rotor could give a measure of the internal damping. They showed that internal friction is amplitude dependent. They performed rotating tests, which showed that the rotor would go unstable at high speeds, and modeled the rotor-bearing system with XLTRC, a computer code, in an attempt to predict the threshold speed. Their foundation model used synchronous force coefficients.

CHAPTER III

BASICS OF INTERNAL ROTOR DAMPING

Friction is generated between any two bodies in contact with each other, moving or tending to move in opposite directions. Damping, a more general term, is the process by which the amplitude of vibration steadily decreases [17]. The energy is dissipated in the form of friction or heat. The various forms of damping are viscous, coulomb and hysteretic damping.

Viscous damping arises from fluid interaction, in which the damping is proportional to the velocity. In a viscously damped harmonic motion, the successive amplitudes have a logarithmic relation with one another. The viscous damping can be found from the logarithmic decrement. Coulomb or dry friction damping is caused due to the kinetic energy dissipated between sliding surfaces. Hysteresis or solid damping is caused by the internal friction when a solid is deformed, and is independent of frequency.

In rotating systems, external friction or damping tends to stabilize the system. Internal damping in rotors is destabilizing. It can be generated by the different layers of the material tending to slide across each other when the shaft rotates. The energy dissipated over a cycle in viscous damping is frequency dependent (increases with increase in frequency). A viscous damping model is not an accurate representation of internal damping.

The energy dissipated in a hysteretic model is frequency independent or slightly decreases with increasing frequency and is a more realistic representation of the internal damping. The internal hysteretic damping can be represented by assuming the damping force to be directly proportional to the velocity and inversely proportional to the frequency. The constant h that is replaced by $c_i w$ is called the hysteretic constant [17].

$$h = c_i w \qquad \textbf{Eq 3. 1}$$

Hysteretic damping can be converted to logarithmic decrement using Eqn 3.2.

$$d = \frac{p\ h}{M_{eq}\ w_d^2} = \frac{p\ h}{K}$$ **Eq 3. 2**

where d = logarithmic decrement of the system

m_{eq} = equivalent mass of the system

w_d = damped natural frequency of the system

The traditional mass-spring-damper system uses a viscous damping element with the damping force proportional to the velocity. In order to be able to use this model, the hysteretic or coulomb damping is converted to an equivalent viscous damping.

Internal rotor damping is stabilizing at speeds below the critical, but at speeds above the critical it creates a disturbing force that destabilizes the system. The rotor begins to whirl at a speed equal to the first critical speed, independent of the shaft speed. The beginning of the whirling motion is marked by the occurrence of a subsynchronous component of vibration on the waterfall plot.

The subsynchronous component can occur either during runup or coastdown or both. The phenomenon of the frequency splitting into a synchronous and a non-synchronous frequency due to an instability is called as instability bifurcation. If the subsynchronous components occur only during the runup tests and not during the coastdown tests, it is called super-critical bifurcation [18]; and if it occurs only during the coastdown tests it is called sub-critical bifurcation. Often tests show that the rotor starts showing subsynchronous components above a certain speed during the runup test, but during the coastdown the subsynchronous components do not disappear until a speed which is lower than the speed at which the components appeared during the runup tests.

Internal friction theory of shaft whirl

To understand the internal friction theory of shaft whirl, let us assume a uniform shaft with a disk at the mid span, deflected by gravity (Fig 1).

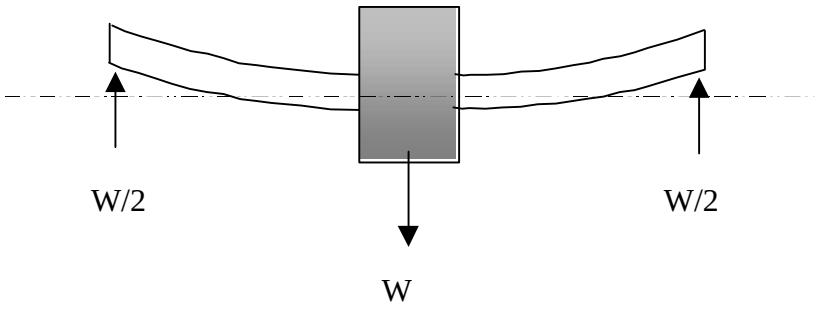

Figure 1: Model to explain shaft whirl due to internal friction

The shaft can be assumed to be composed of layers of fibers. Looking at the bent-static disk-shaft system in the front view as shown in Figure 1, the fibers at the bottom of the shaft are in compression while the layers at the top are in tension. As this bent shaft rotates, the rate of change of extension or compression on the fibers induces an internal friction within the layers (as opposed to the elastic stresses that depend on the amount of extension or compression). This internal friction produces a tangential force on the system that makes it spring forward (elastic stresses tend to make the shaft spring upwards). This transverse force sets the shaft into a whirl motion.

Using an equivalent viscous model for the damping, the tangential force created due to the whirling of the shaft is given by:

$$F_{\tan} = c_i (w - \dot{f}) r \qquad \textbf{Eq 3. 3}$$

where c_i = coefficient of internal damping

w = shaft rotating speed

r = whirl radius

$\dot{f}$ = whirl speed

This equation shows that for speeds $w < \dot{f}$, the force is negative, and hence damps out the vibration. But for speeds $w > \dot{f}$, the force tends to set the shaft in a whirl and the vibration amplitude gets larger with time, thus driving the system unstable.

The natural whirling speed of the system of the system is the damped natural frequency w_d. For light external damping, w_d will approximately be equal to the critical speed of the system w_{cr}. Hence the destabilizing tangential force can be written as

$$F_{\tan} = c_i (w - w_{cr}) r \qquad \textbf{Eq 3. 4}$$

Procedure to determine internal damping

Internal damping in a system can be determined by hanging the rotor free-free and rapping to get the logarithmic decrement of the system. Mir [16] and Khalid [15] had done rap tests on the disk-shaft system studied here and had determined the logarithmic decrement from which an equivalent viscous damping was determined. One of the concerns in a rap test is to simulate the running speed peak amplitude and the only way of doing this is to rap the rotor hard enough so that the peak due to the impulsive force of the hammer is comparable with the running speed peak amplitude.

In order to simulate the running speed amplitudes in a static test, a shaker, capable of exerting about 30 lb force over a range of frequencies is a good alternative to the rap tests. Hence a shaker was used in this thesis to excite the rotor, and parameter identification was carried out by analyzing the frequency response of dynamic stiffness transfer functions (F / X). Models were developed and the validity of the test results was confirmed by correlating the results with the mathematical model and the XLTRC2 model.

CHAPTER IV

DESCRIPTION OF TEST RIG

The test rig donated by Shell Oil Co. (Figure 2.) was used for the experiments.

Figure 2: Test rig

A single disk rotor with a taper sleeve arrangement was used to vary the interference fit. The rotor assembly weighs 79.5 kg (175 lb) and is 1.32 m (52.25”) long. The shaft diameter is 63.5 mm (2.5”). The wheel diameter is 254 mm (10”) and is 127 mm (5”) long. The wheel resides at the center of the shaft. The shaft is supported on ball bearings; the bearing span is 1.07 m (42”).

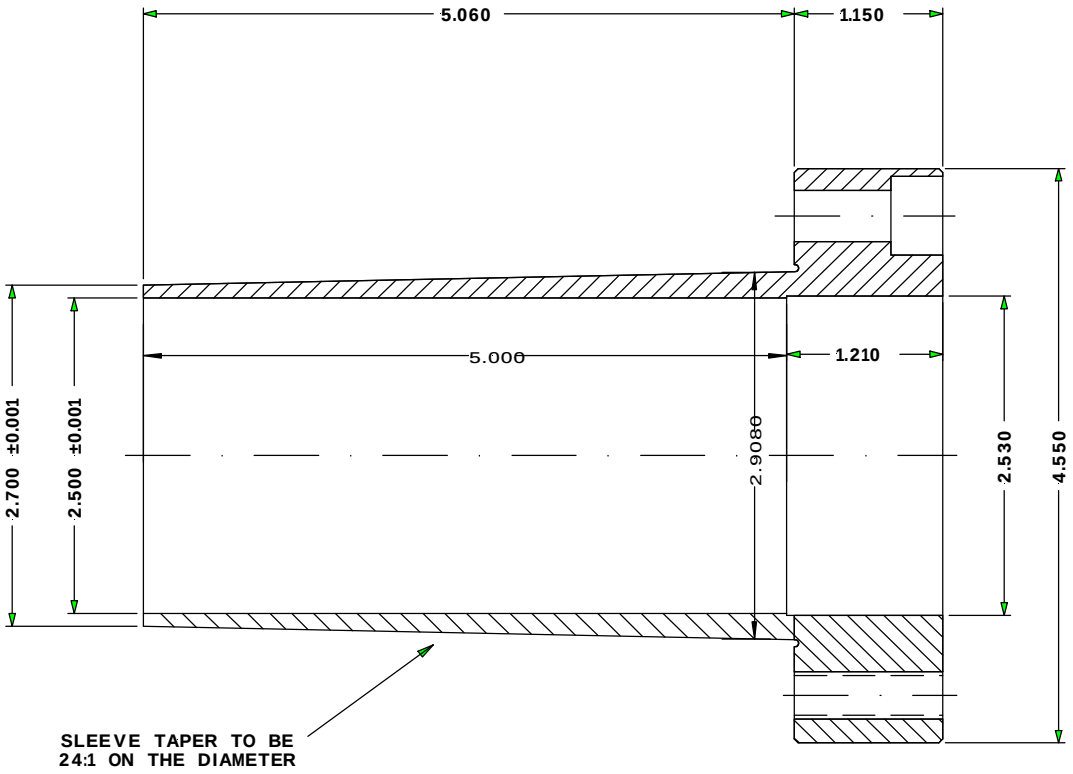

Figure 3: Taper sleeve

Adjusting the interference fit

The taper sleeve arrangement is shown in Figure 3. The taper in the sleeve is 1/24. The disk is mounted on the tapered portion of the sleeve. The Allen bolts that connect the sleeve and the disk are used to vary the interference between the two elements. These bolts are arranged equi-spaced along the periphery of the sleeve; there are a total of 12 bolts. The fit can be made more or less tight by tightening or loosening the draw and the push bolts that are shown in Figure 4. A measure of the interference is given in terms of D, denoted in Figure 4. From the geometry of the disk, the distance D that gives zero interference is 39.1668 mm (1.542”), and is denoted by S. The formula to calculate the radial interference is

$$If = \frac{T}{2}(S - D) \qquad \textbf{Eq 4. 1}$$

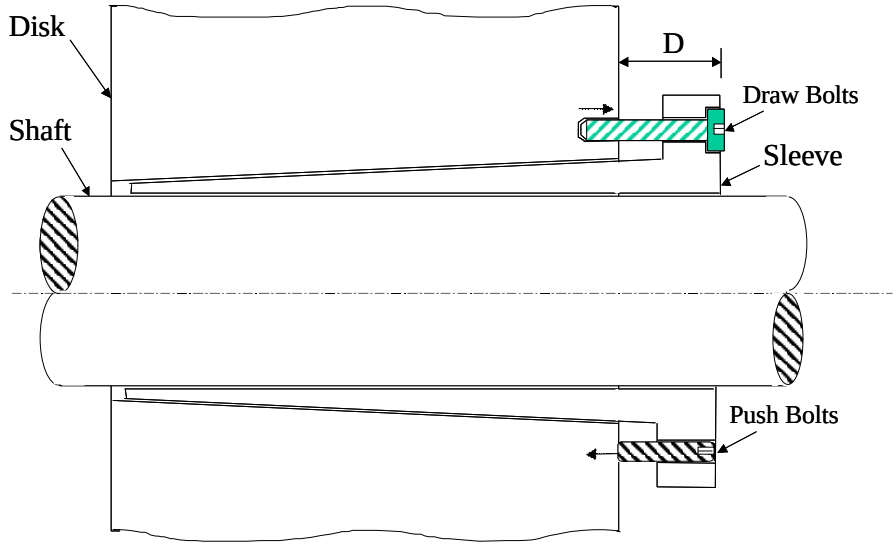

Figure 4: Sleeve-shaft assembly

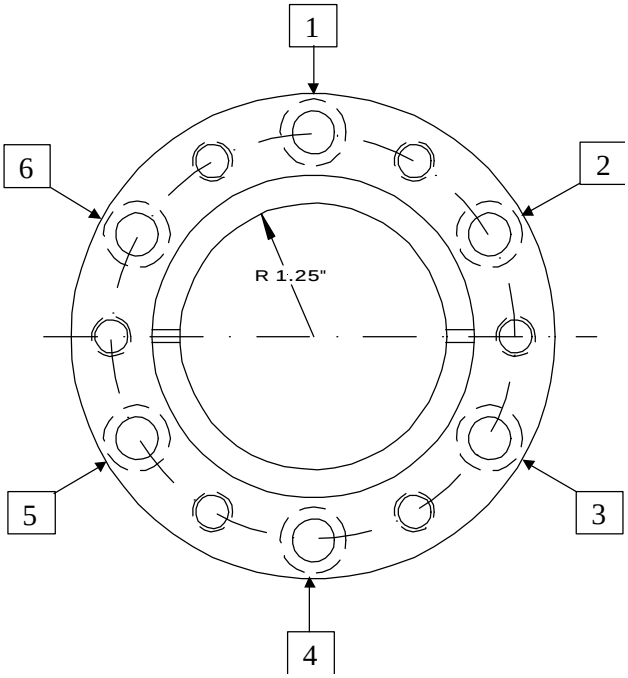

Figure 5: Positions where the axial distance is measured

where T is the taper ratio and is 1/24. Substituting these values in the equation, we get the following equations.

$$If_{English} = 0.02083 \cdot (1.542 - D) \text{ inches}$$

$$If_{SI} = 0.02083 \cdot (39.1668 - D) \text{ mm}$$

In order that the value of D be constant throughout the periphery (and thus give a uniform interference fit all around), the distance was measured at six locations (shown in Figure 5) and the average was taken to get the interference. A digital vernier with a least count of 0.0127 mm (0.0005”) was used for the measurements.

Parts of the test rig

The major parts of the test rig consist of the drive train and the instrumentation. The drive system is a 30 hp variable speed motor that is connected to a jackshaft via a toothed belt that has a speed ratio of 1 to 4.8. The jackshaft is mounted on two 5-pad tilt pad bearings. This is connected to the rotor by a flexible coupling. The main rotor bearings are SKF 1215 K double row self-aligning ball bearings. There are 20 balls at each row and the ball diameter was 0.5 inch (12.5 mm). The bearings are lubricated by a pressurized lubrication oil system. The two bearings are mounted on split-type SAF 515 pillow block housing.

The instrumentation consisted of 8 mm Bently Nevada non-contact eddy current proximity probes mounted on probe pedestals close to the mid span of the shaft. The key phasor (which is also an 8 mm non-contact eddy current probe) was mounted 15^{0} from the vertical axis. The key phasor measures the phase and the angular speed of the shaft.

The probes were powered by 24 V Dymac proximitors. These were connected to a Bently Nevada ADRE 208 data acquisition system for gathering and storing the running test data. An oscilloscope was used to see the real time unfiltered orbit. A HP dynamic signal analyzer was used to display the frequencies during the running test.

CHAPTER V

EFFECT OF FOUNDATION STIFFNESS ON THRESHOLD SPEED

Literature [5] shows that the onset speed of instability (OSI) depends on the foundation stiffness; the OSI is lower for a foundation with symmetric stiffness along the horizontal and the vertical directions, as compared to an asymmetric one. One objective of this thesis is to study the effect of increase in the horizontal stiffness of the foundation (thus making it more symmetric) on the OSI due to internal friction. Another objective is to differentiate benign from potentially unstable subsynchronous vibrations. Ferrara [19], working with high speed compressor units, has suggested that subsynchronous vibration does not always indicate instability. This chapter enumerates experiments done by stiffening the foundation horizontally. Rap tests previously done by Mir [16] and Khalid [15] showed that the horizontal and vertical natural frequencies are 40 Hz and 52 Hz. They also showed that at some values of low interference fit, the system became unstable at high speeds, while no instability was noted for tighter fits.

Stiffening the foundation

In this thesis, the word “foundation” refers to the welded steel structure supporting the bearing housing. It is anchor bolted to the concrete floor. To study the effect of increase in the horizontal foundation stiffness on the onset speed, a hardware arrangement was made as shown in Figure 6. An I-beam built section anchored to the floor was used as a support to pull on the foundation. The I-beam was bolted close to the bearing. An eye bolt was connected to the foundation. A 6.35 mm (¼”) diameter galvanized steel guy wire wrapped around thimbles was connected on one end to the eye bolt on the foundation. The other end was connected to a turn buckle that was mounted to the I beam section. This arrangement facilitates increasing the stiffness of the foundation along the horizontal direction, as the turn buckle is tightened. To get a measure of the stiffness, pull tests were performed and the deflection of the foundation was noted. A dial gauge with a precision of 25.4 μm (0.00001”) and an Omega force gauge were used for the measurements. Since the bearing pedestal is attached to the foundation, pulling on

Figure 6: Arrangement to constrain the foundation

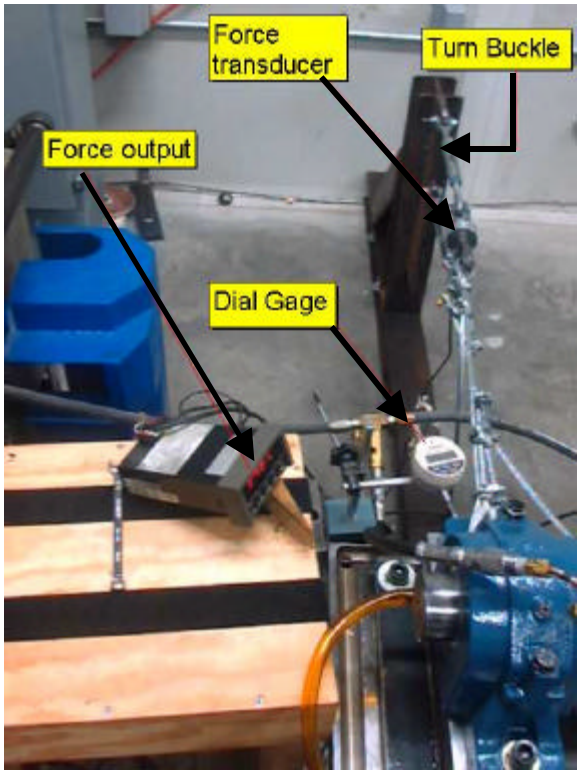

Figure 7: Arrangement to measure the foundation stiffness

the bearing pedestal would result in a deflection of the foundation. A thimble was secured to the bearing housing, and the steel guy wire was routed through this thimble. This wire was connected to the force gauge, as shown in Figure 7.

The turn buckle was used to tighten the cable, and the deflection and force gauge readings were noted. The cable was tightened to the maximum possible extent, considering the practical aspects of the cable not breaking and the I-beam not cracking out of the floor. The force versus deflection curve for the foundation without tightening the cable is shown in Figure 8.

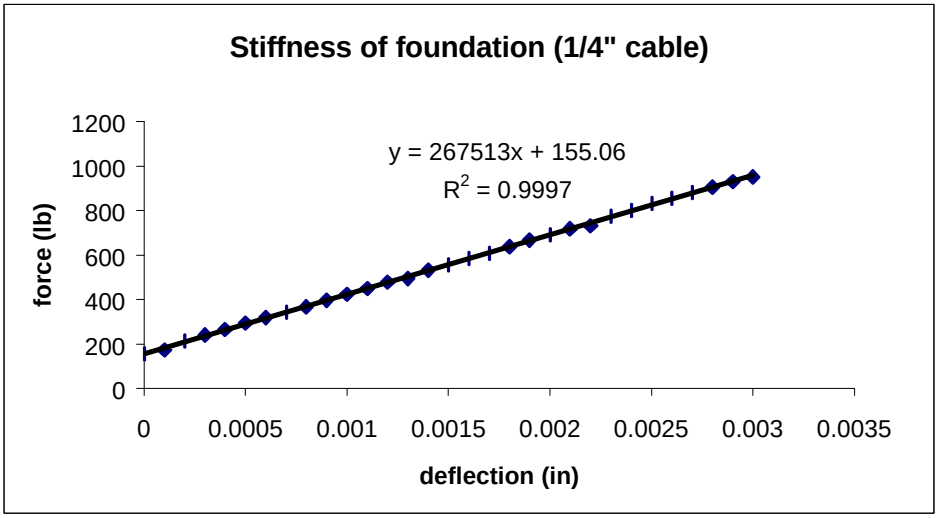

Figure 8: Force vs deflection curve for the foundation stiffness (case 1)

A 9.53 mm (3/8”) diameter steel cable was used, and it was found that the stiffness could be increased to 1.26 times the foundation stiffness. This value was 59.17 MN/m (337750 lb/in). This is shown below in Figure 9. The 3/8” diameter cable was used for further testing.

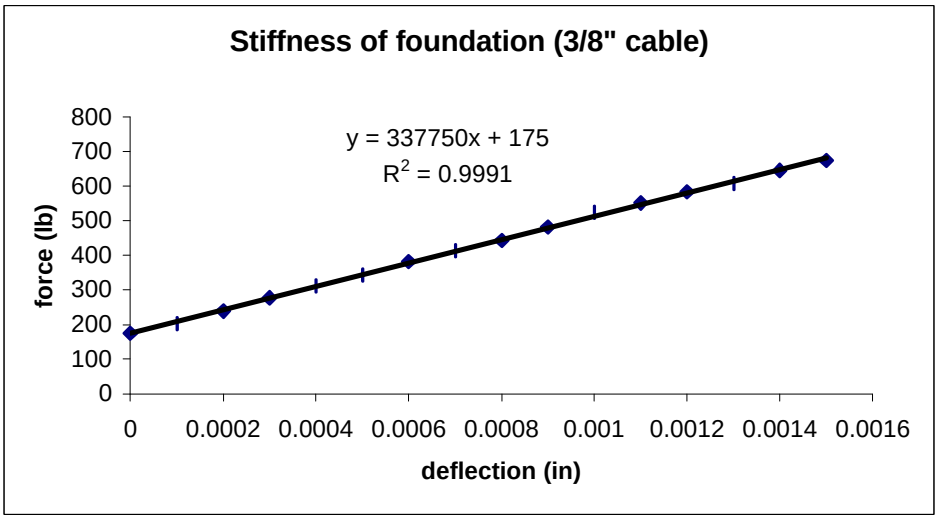

Figure 9: Force vs deflection curve for the foundation stiffness (3/8" cable)

Running tests

Tests were performed by running up the rotor to a top speed of around 9000 rpm and allowing it to coastdown. The runup and coastdown data were captured in ADRE and the plots were analysed. A number of cases were analyzed, and the results are presented in the following pages.

Base case

Figure 10 shows the cascade plot of the x probe for the base case without stiffening the foundation. The interference of 8.76 μm (0.345 mils) is a very small. It can be seen that the rotor goes unstable at around 7140 rpm. The data also reveal that the rotor becomes unstable only during the coastdown. After the testing was over, it was found that the disk had moved from its initial position. The movement of the disk indicates that it had become completely loose at high speed; however the subsynchronous vibration occurs only during the coastdown and at a speed less than maximum shaft speed.

Foundation stiffened on one end

Initial tests were done by stiffening the foundation on one side and at one end. The interference was kept around 10.16 µm to 15.24 µm (0.4 to 0.6 mils) and the data were acquired. Figure 11 shows the cascade plot of the X probe for an interference of 14.98 µm (0.59 mils). No subsynchronous vibration is noted.

Foundation stiffened on both sides

Several runs were made with the foundation constrained on one end. The data were similar to that shown in Figure 11. No subsynchronous component was noted. Thereafter, the other end of the foundation close to the driving end, was also constrained using a similar hardware arrangement with 3/8" diameter steel cables and the tests were repeated. Figure 12 shows the cascade plot. According to theory [4] the subsynchronous vibration should have occurred at a

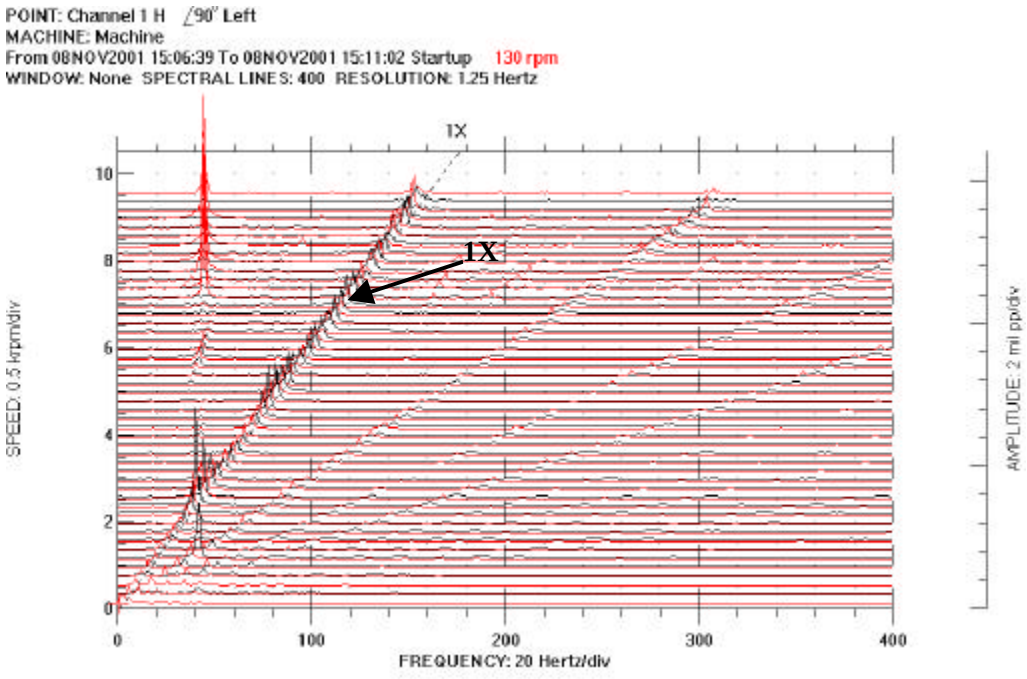

Figure 10: Cascade plot of X probe for base case

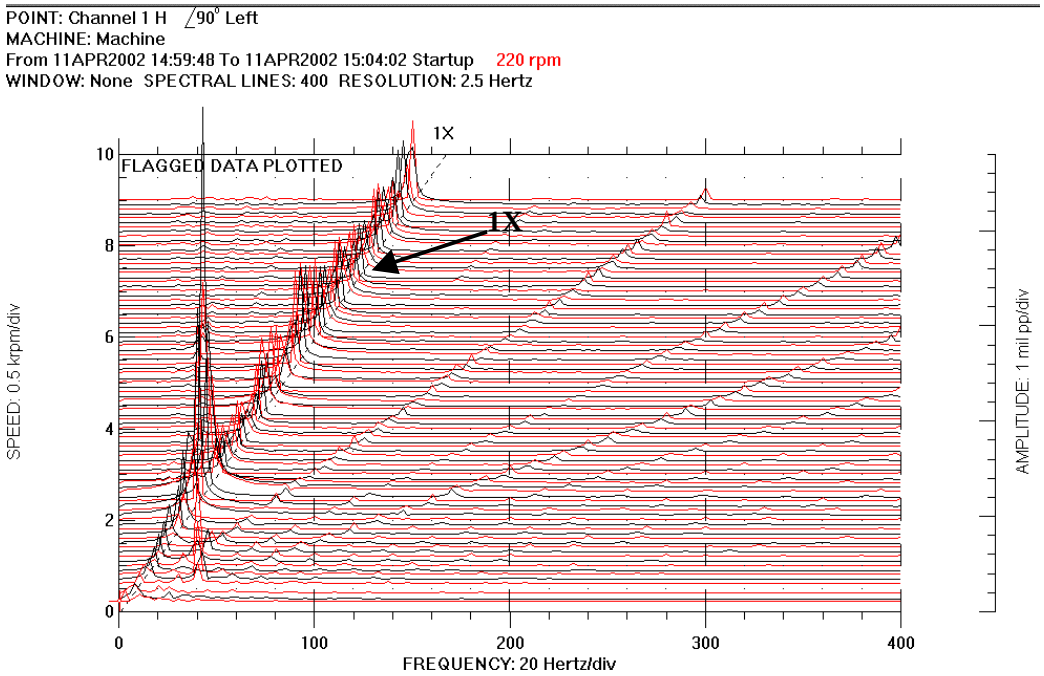

Figure 11: Cascade plot of X probe with one end of foundation stiffened

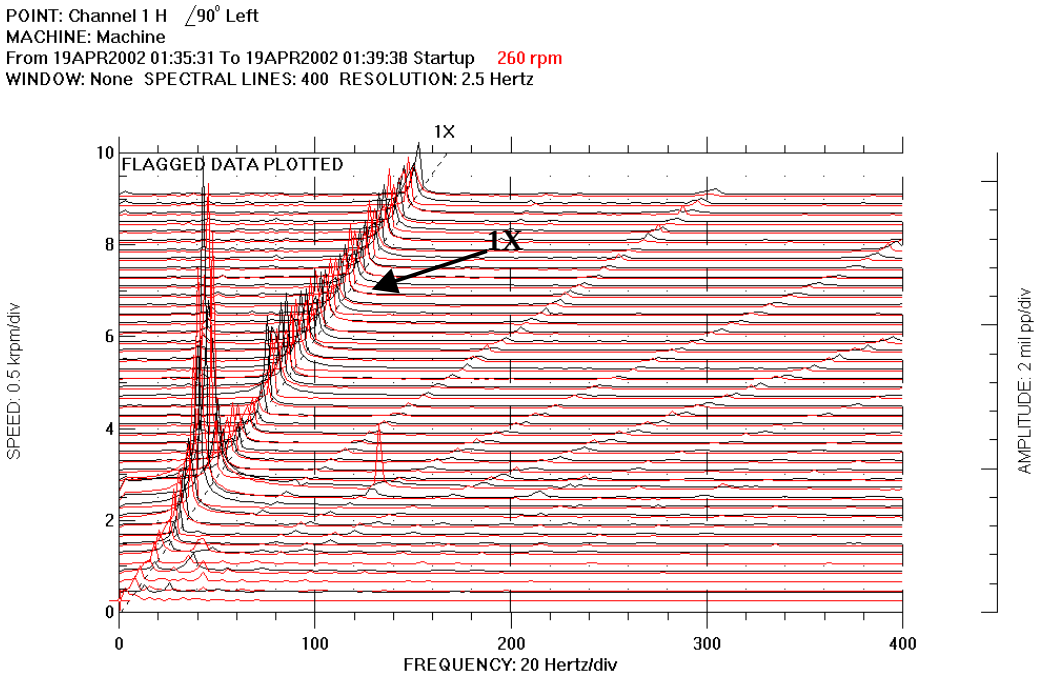

Figure 12: Cascade plot of X probe with both ends of foundation stiffened

lower shaft speed (compared to the base case) when the foundation stiffness was increased and made more symmetric, but in fact it disappeared.

Effect of balancing

Using a linear mathematical model, Vance and Lee [8] showed that the threshold speed of instability due to internal friction is the same for both balanced and unbalanced rotors. Since no subsynchronous frequencies were noticed while unbalanced (Figure 12), balance screws were added to the rotor as follows: A 7.93 mm (5/16") screw weighing 15.58 grams was used to balance the shaft, and brought down the synchronous response peak (at the mid-span) from 0.69 to 0.43 mm (27 mils to 17 mils). Subsynchronous frequencies were then observed at rotor speeds close to 5300 rpm and 8900 rpm, thus contradicting the linear theory. The waterfall plot is shown in Figure 13. It can be observed from these graphs that subsynchronous frequencies occur at rotor speeds close to 5300 rpm and 8900 rpm during the coastdown. A plot of the frequency

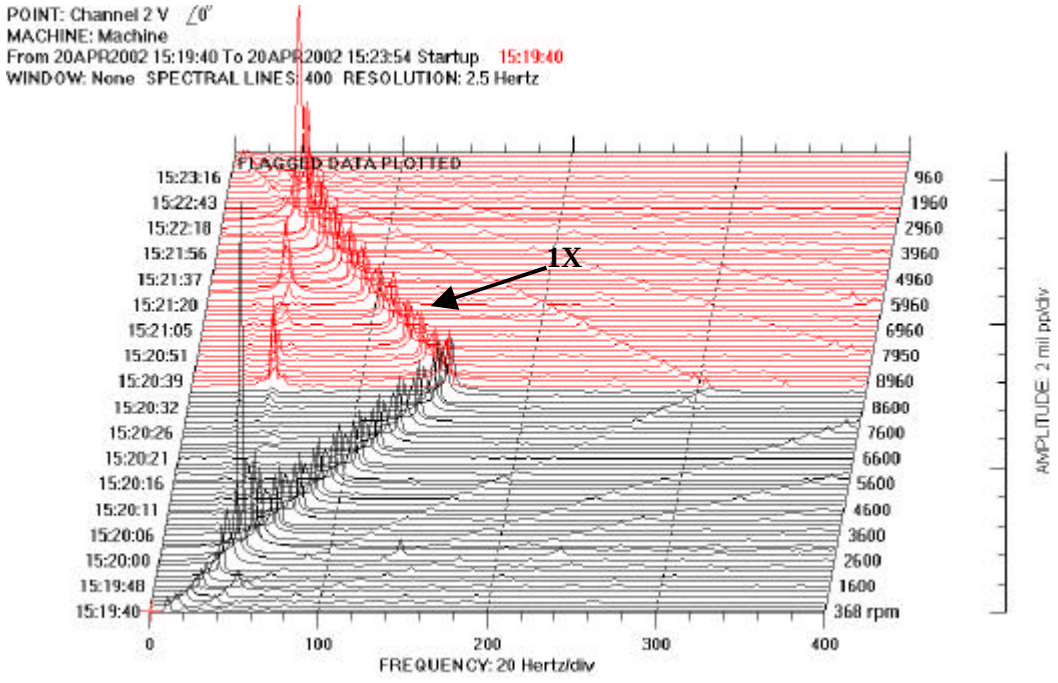

Figure 13: Waterfall plot of Y probe with balance mass added and foundation stiffened

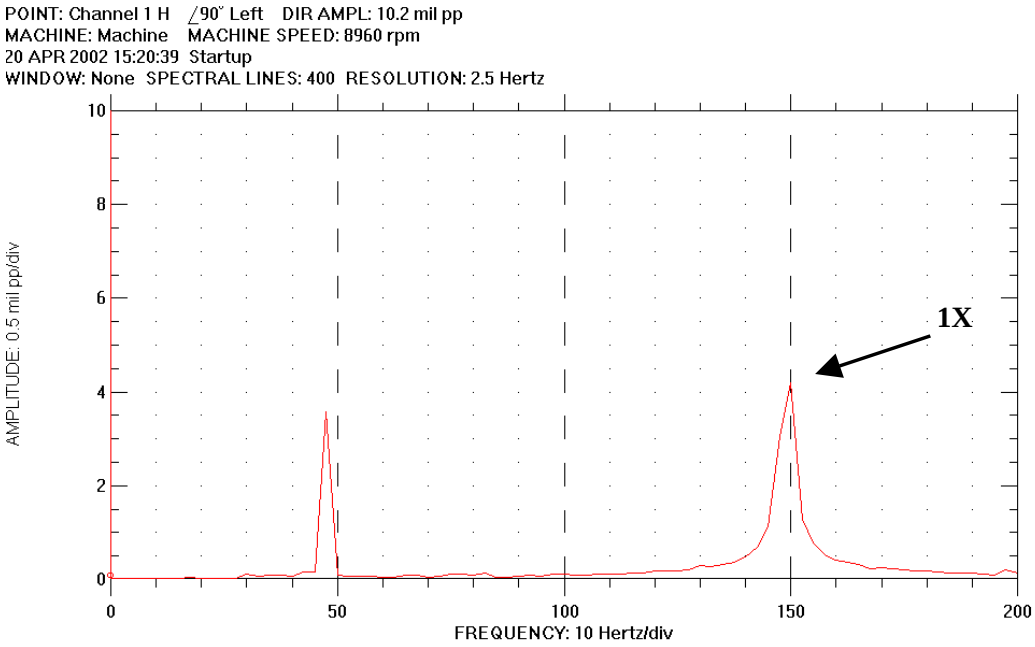

Figure 14: X probe frequency spectrum at 8960 rpm

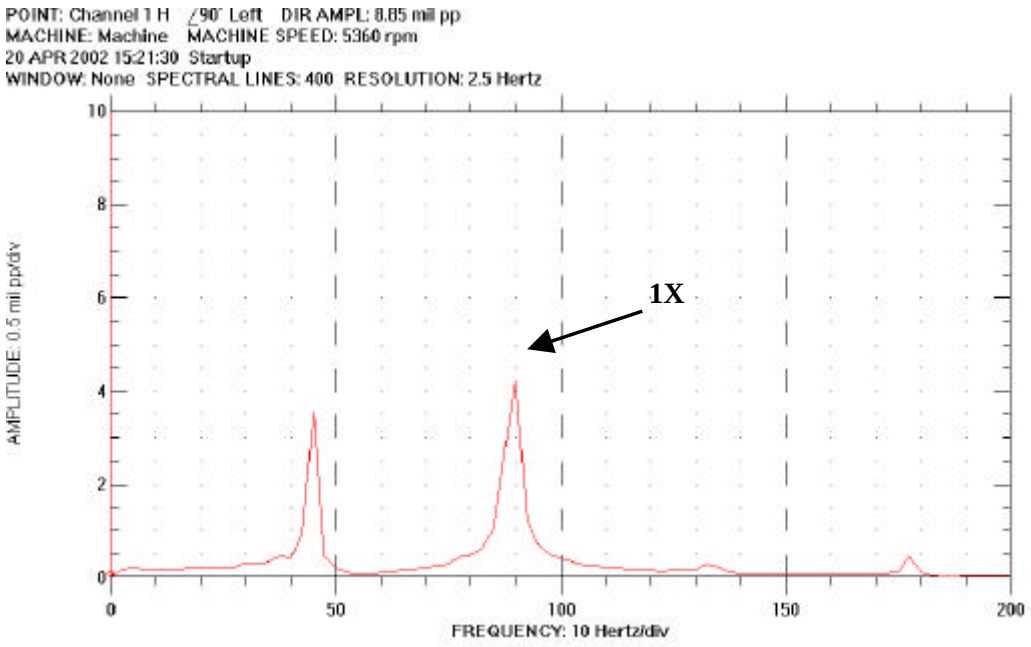

Figure 15: X probe frequency spectrum at 5360 rpm

spectrum at 8960 rpm and 5350 rpm is shown in Figures 14,15. The subsynchronous components at 8960 and 5360 rpm appeared after the addition of the balance screw. Gunter [20] reported similar experimental results where balancing made oil whirl more severe. These results contradict the prediction of the linear model of Vance and Lee [8].

Addition of anti-seize compound

To avoid seizure of the mating parts due to interference fit in rotors, common industry practice is to apply an anti-seize compound on the surfaces in contact. To simulate this condition and investigate its effect on rotordynamic stability, anti-seize compound was applied on the sleeve so that as the disk slides on the sleeve, the anti-seize compound action comes into play. The same type of signatures were noted for the tests with and without the anti-seize: the anti-seize had no effect. The running tests were done with and without the balance screw. With the balance mass attached, subsynchronous frequencies were noted over a small range of speed. The results shown

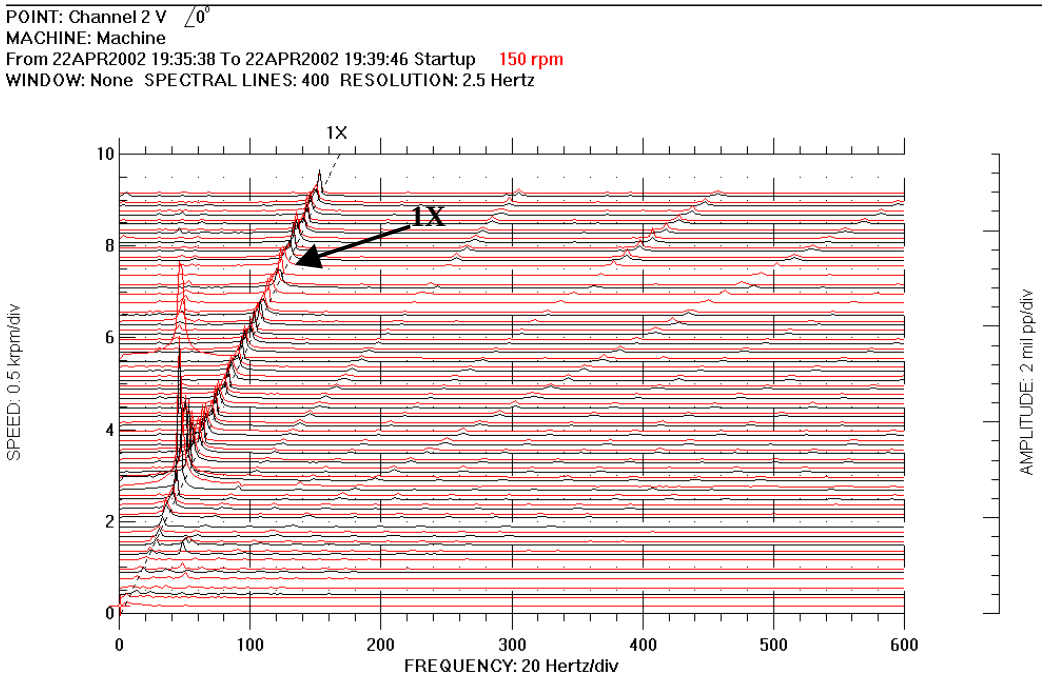

Figure 16: Y probe cascade plot with anti-seize applied and with balanced mass

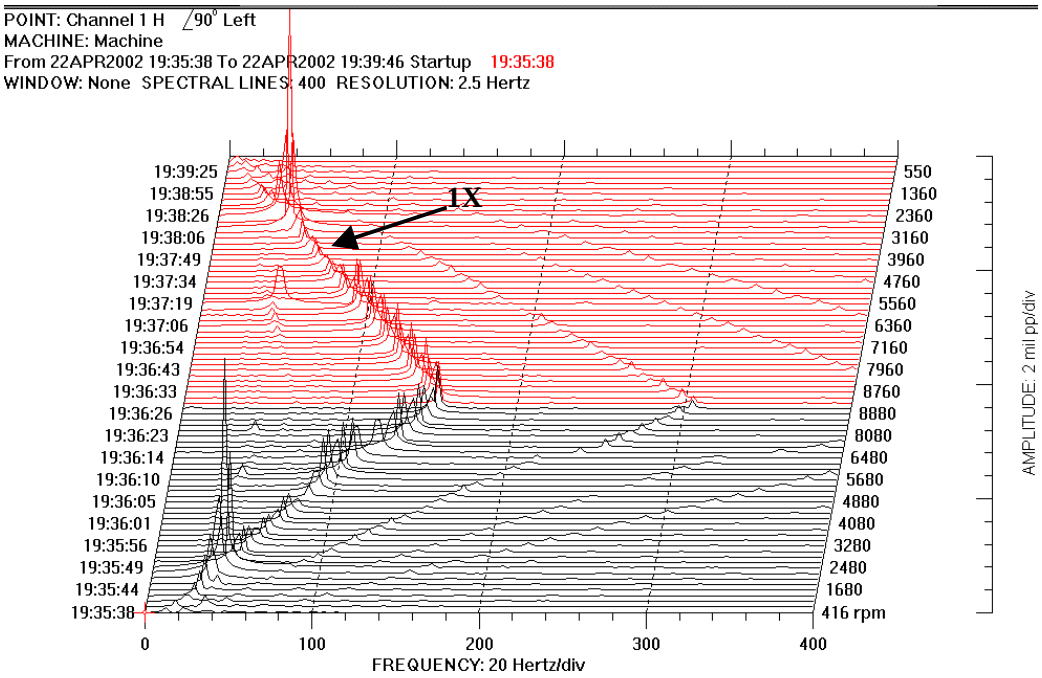

Figure 17: Y probe waterfall plot with anti-seize applied and with balanced mass

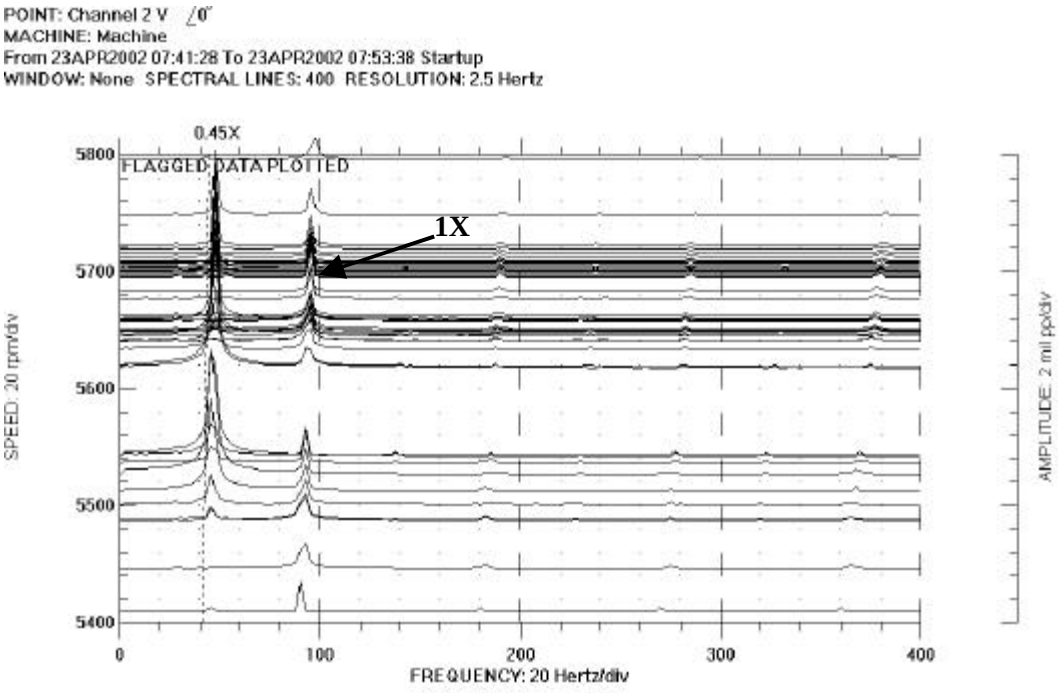

Figure 18: Y probe cascade plot for machine hovering around 5700 rpm

in Figures 16,17 are for tests done with the balanced rotor and with the anti-seize compound added. The waterfall plots reveal that these peaks occur only in the coastdown. Several runs had to be made to ascertain that the subsynchronous vibration was really at this speed. Since there is a high probability of missing the signal due to rapid acceleration or deceleration rate of the machine, the tests were done by hovering the rotor at speeds near 5700 rpm; test data were collected every 0.5 seconds in ADRE.

Hovering speed data

These tests were done with the anti-seize compound and the balance mass added, with the rotor made to decelerate slowly from 6200 to 5400 rpm. The cascade and waterfall plots are shown in Figure 18,19. Strong subsynchronous signatures can be noted.

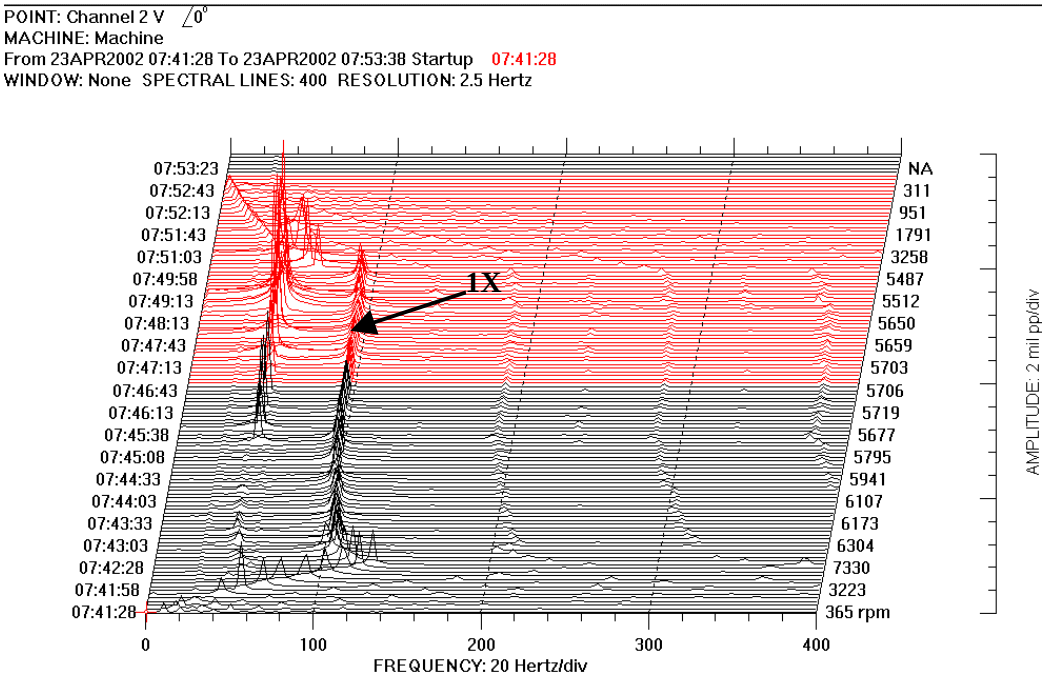

Figure 19: Y probe waterfall plot for machine hovered around 5500 rpm

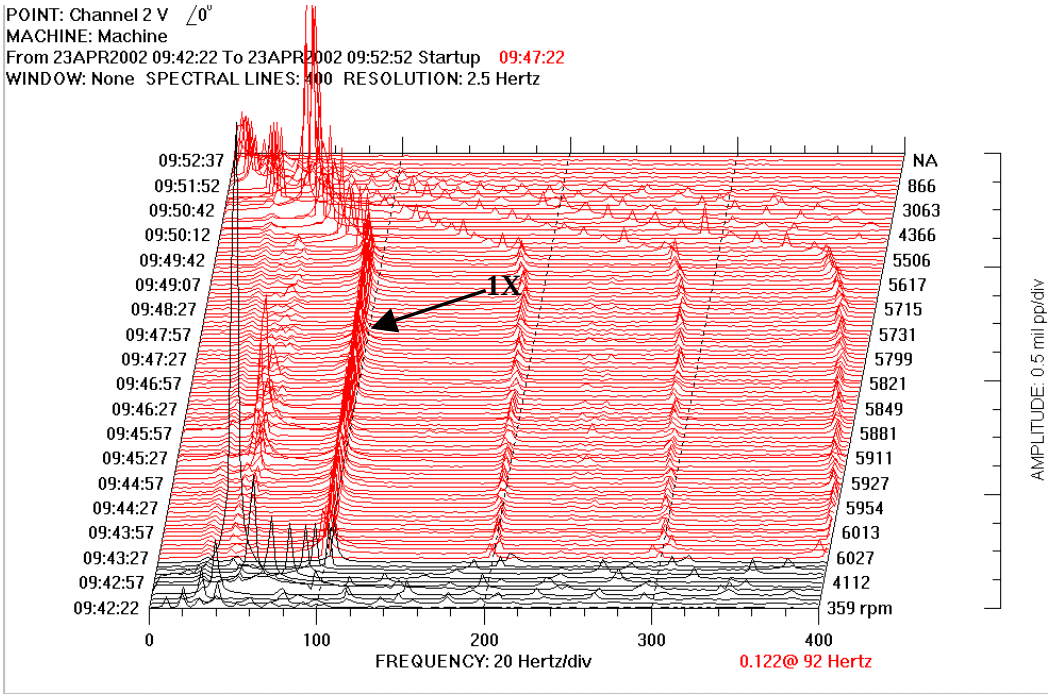

Figure 20: Y probe cascade plot for machine hovered around 5500 rpm for tight fit while balanced

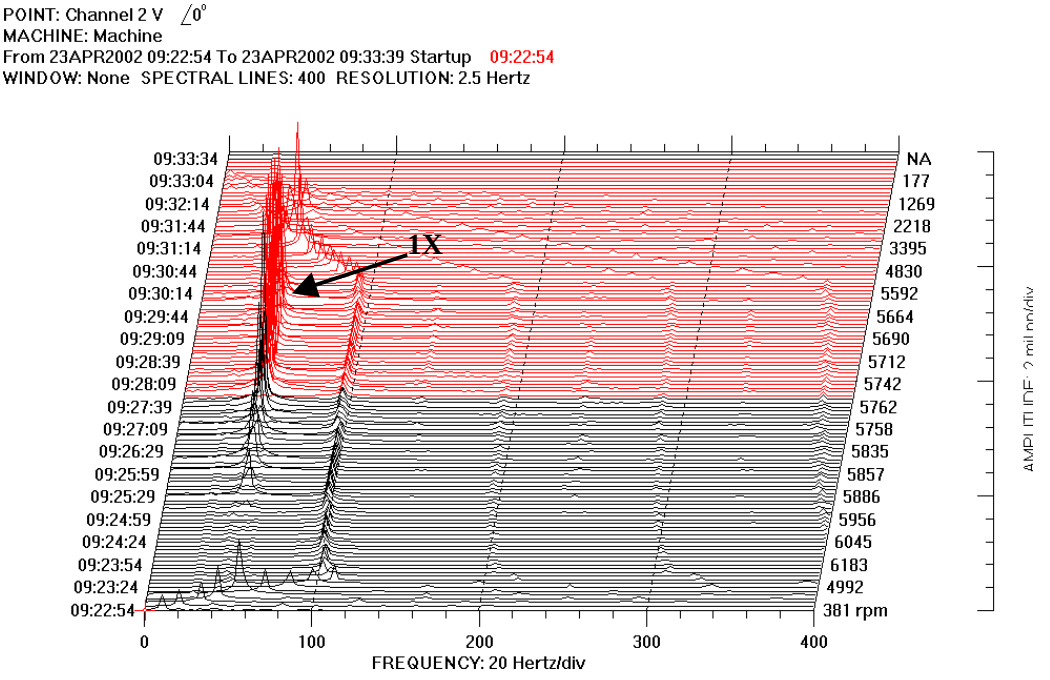

Figure 21: Y probe waterfall plot for machine hovered around 5500 rpm for tight fit while balanced

Tight fit

The fit of the wheel was tightened, increasing the interference to about 0.030 mm (1.2 mils); the tests were repeated with the balance mass. The results are shown in Figures 20, 21. It can be observed that the signatures with both tight and loose fits are similar. The tests were repeated without the balance screws, and the same fractional frequencies were noted as were observed for the tests with a small interference fit. The removal of the balance screw did not change the nature of the vibrations. The result is shown in Figure 22.

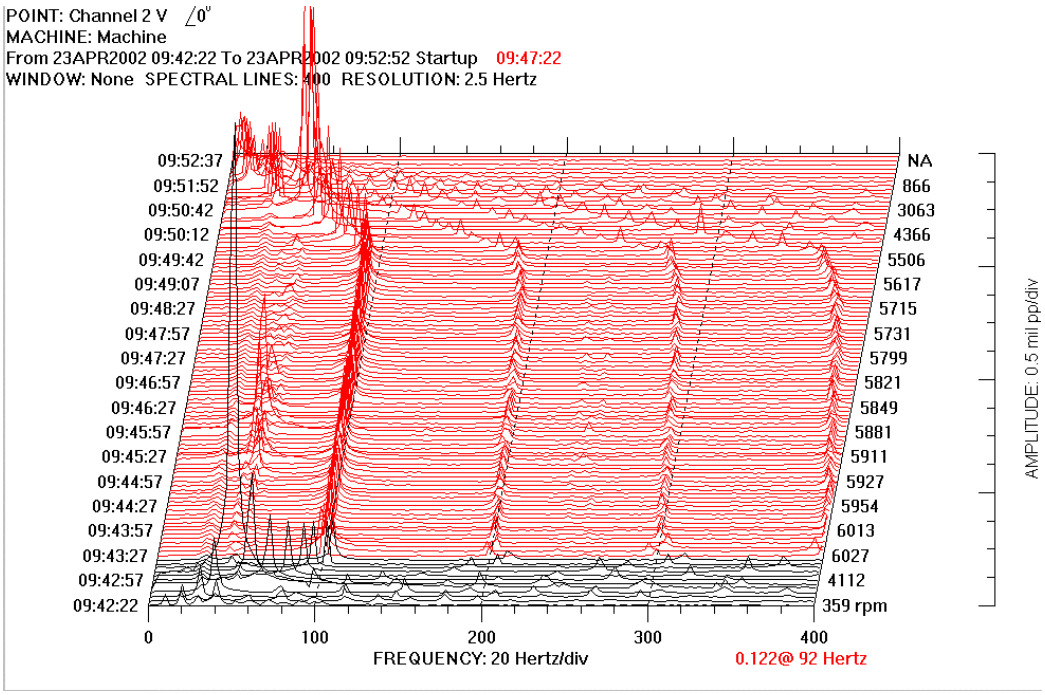

Figure 22: Y probe cascade plot for machine hovering around 5500 rpm for tight fit without balance screws

Belt flapping constrained

It was thought that the drive belt flapping might be the source of the subsynchronous frequencies. To investigate this, a plastic wheel arrangement was made to constrain the movement of the belt; the runs were repeated with the balance screw. Figure 23 shows the hardware arrangement to constrain the flapping of the belt. Figures 24, 25 show the cascade and waterfall plots. The tests were done with the balance screws attached. The subsynchronous vibration is still observed with the belt constrained.

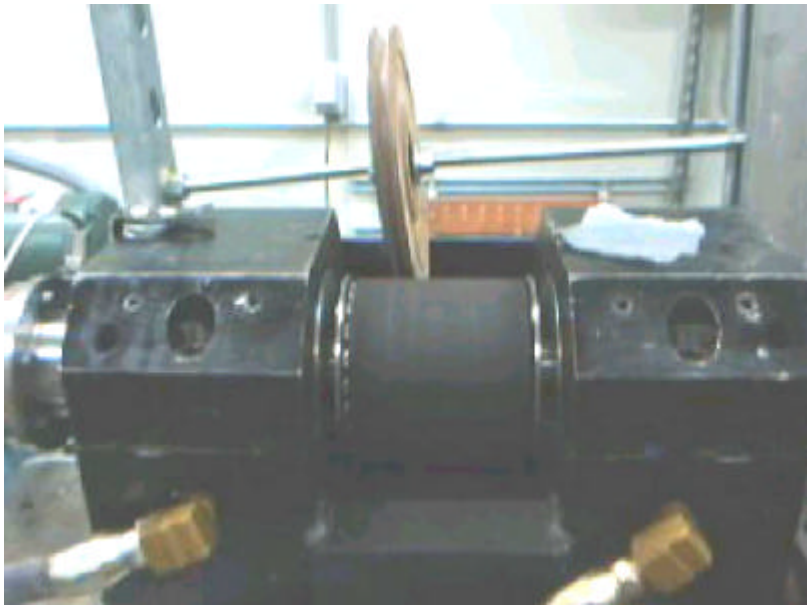

Figure 23: Hardware arrangement to constrain the drive belt from flapping

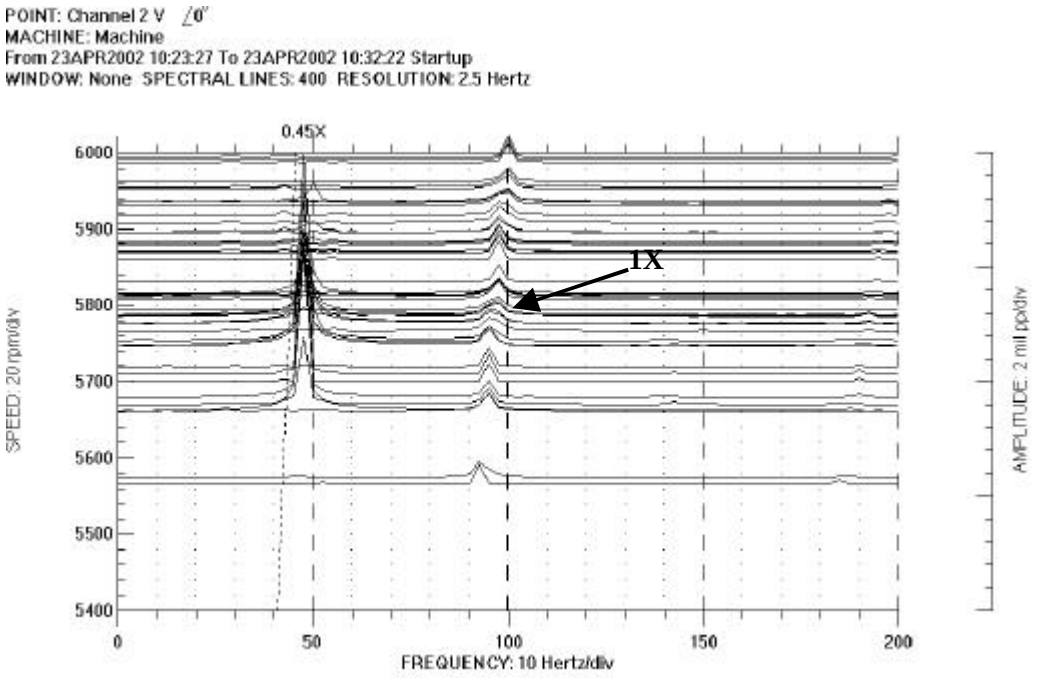

Figure 24: Y probe cascade plot with belt flapping constrained

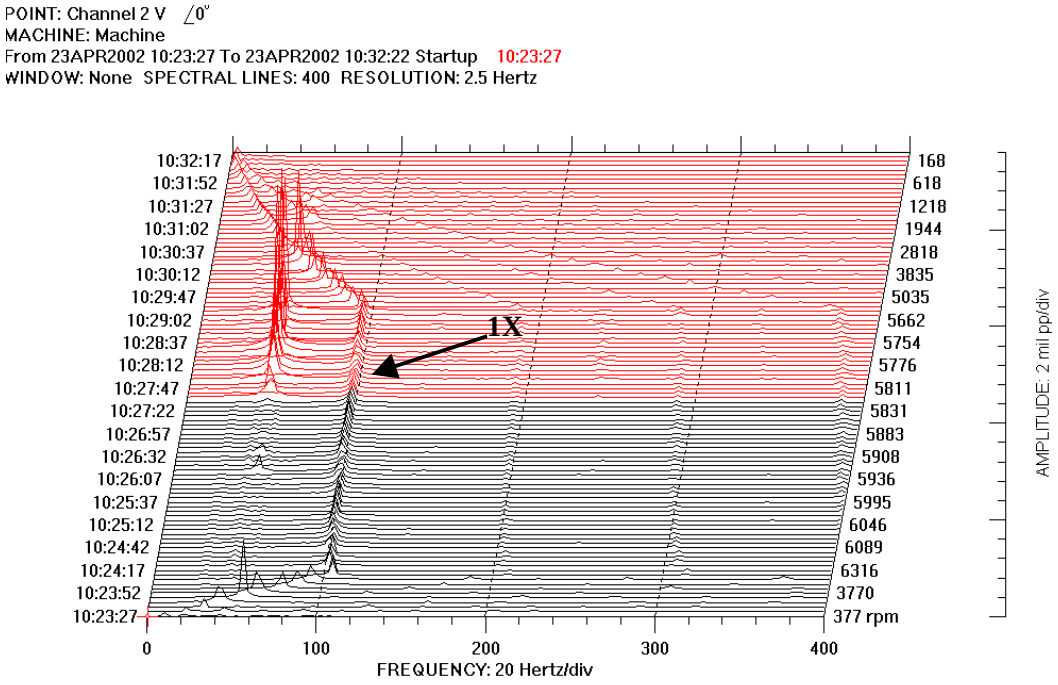

Figure 25: Y probe waterfall plot with belt flapping constrained

Tests with foundation stiffness asymmetry

In order to further investigate the cause of the subsynchronous frequency, and to determine if it is benign or harmful, the foundation constraint was removed and the base case test was repeated, hovering the machine around 5500 rpm. The anti-seize compound was added as before. Tests were done both with and without the balance screw. The results with balance mass are shown in Figure 26, where large subsynchronous vibration is still noted.

Continuing to investigate the cause of the high subsynchronous frequency, the bearing cap was removed and the balls were checked for any damage. No damage was detected in the balls, but it was found that the lock nut which is used to tighten the inner race of the bearing to the shaft (Figure 27) had come loose. This nut was tightened and the tests were done without the balance mass.

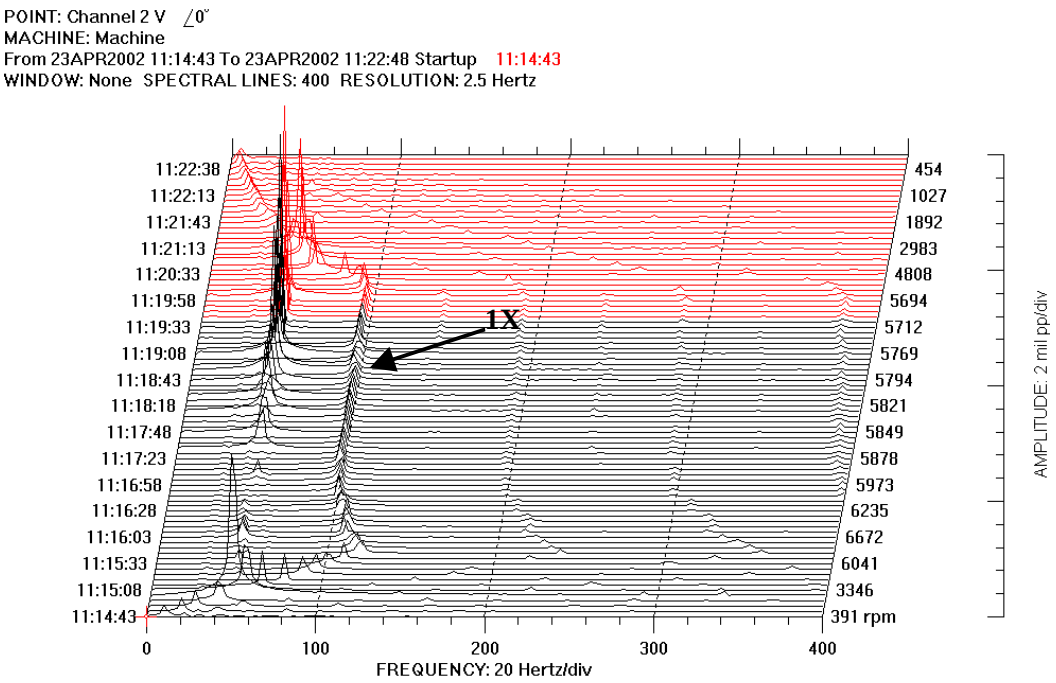

Figure 26: Y probe waterfall plot without stiffening the foundation

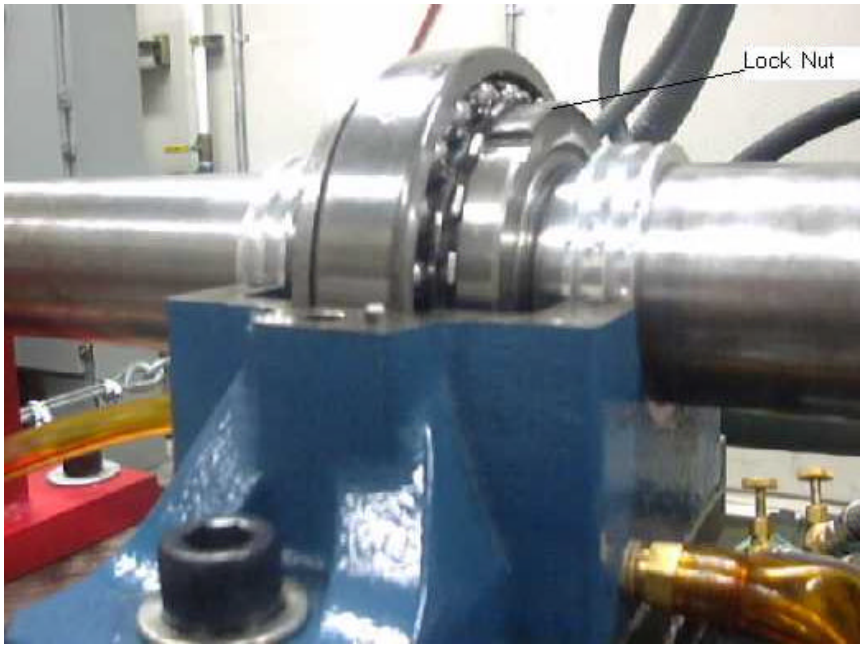

Figure 27: Lock nut that was tightened

Results for loose fit after tightening the bearing lock nut

The runup and coastdown tests were done by observing the spectrum analyzer, and the machine was hovered at speeds where the subsynchronous component was noticed earlier. The waterfall plot is shown in Figure 28. The large subsynchronous frequencies that appeared around 5800 rpm before the lock nut was tightened do not appear now. It can be seen that subsynchronous frequencies now occur in the speed range 5200-5400 rpm and again reappear in the range 6200-6400 rpm. The subsynchronous frequency that appears at the lower speed range is observed to be 0.5 times the running speed. A look at the filtered 0.5X orbit at this speed (shown in Figure 29) shows that it is almost circular. Circular orbits are more prone to instability [21]. However, the tests were repeated with a high interference and the same type of signatures were observed. The cascade plots are shown in Figure 30. Tests were done for a high interference without constraining the foundation, and no significant subsynchronous signatures were observed (Figure 31). The spectrum at 5300 rpm is shown in Figure 32.

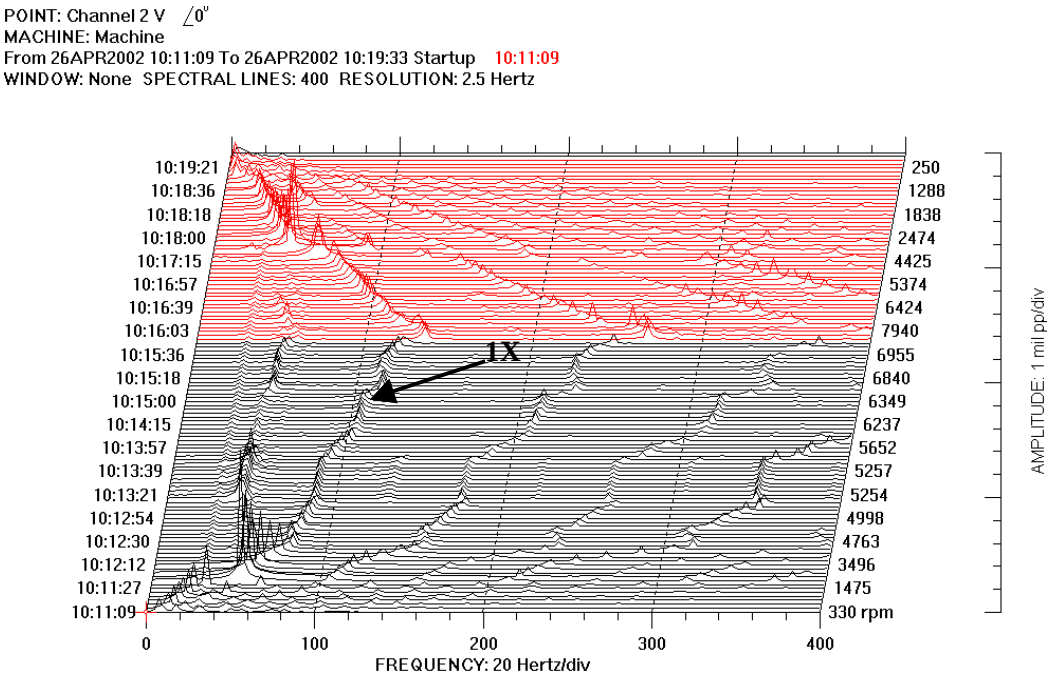

Figure 28: X probe waterfall plot with foundation constrained after lock nut was tightened

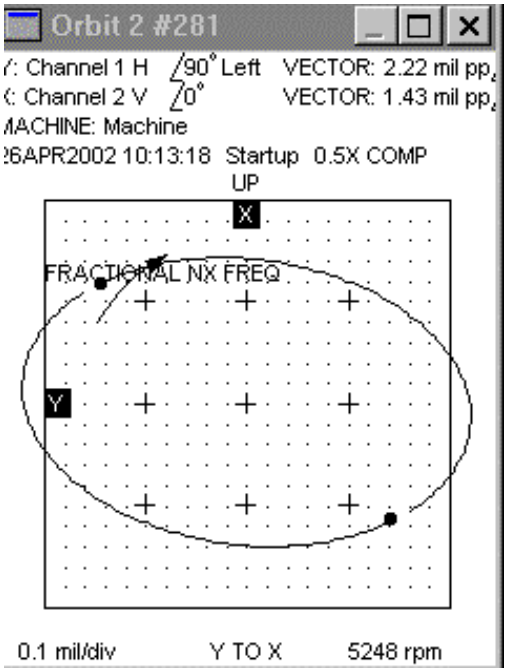

Figure 29: Orbit of 0.5X filtered component at 5200 rpm

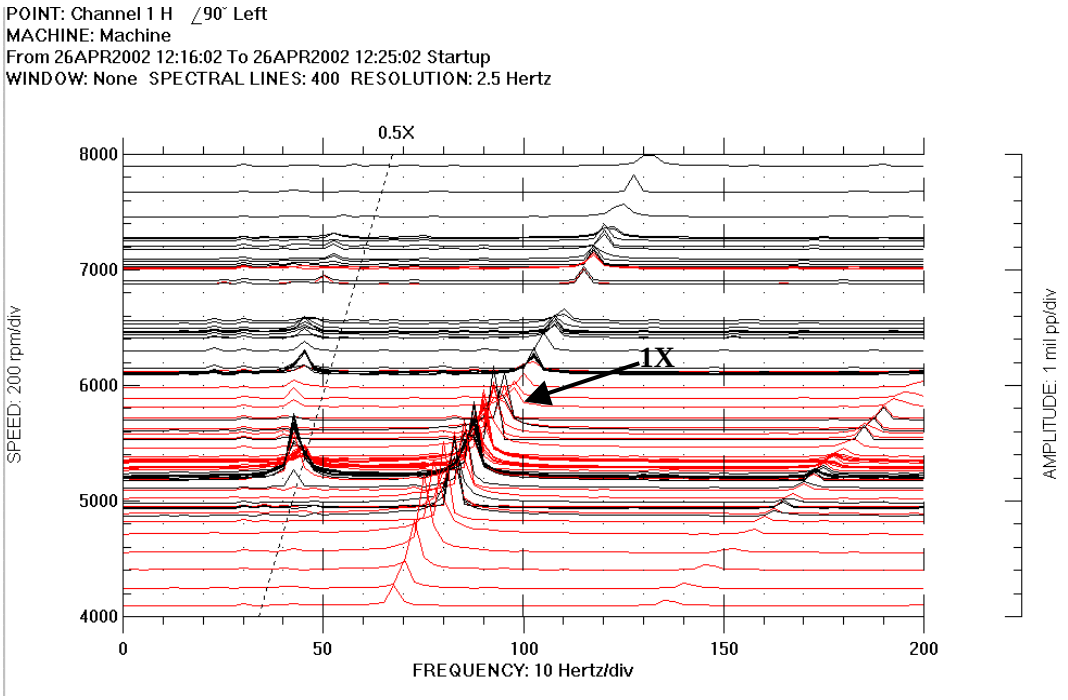

Figure 30: X probe cascade plot for tight fit with foundation constrained after tightening lock nut

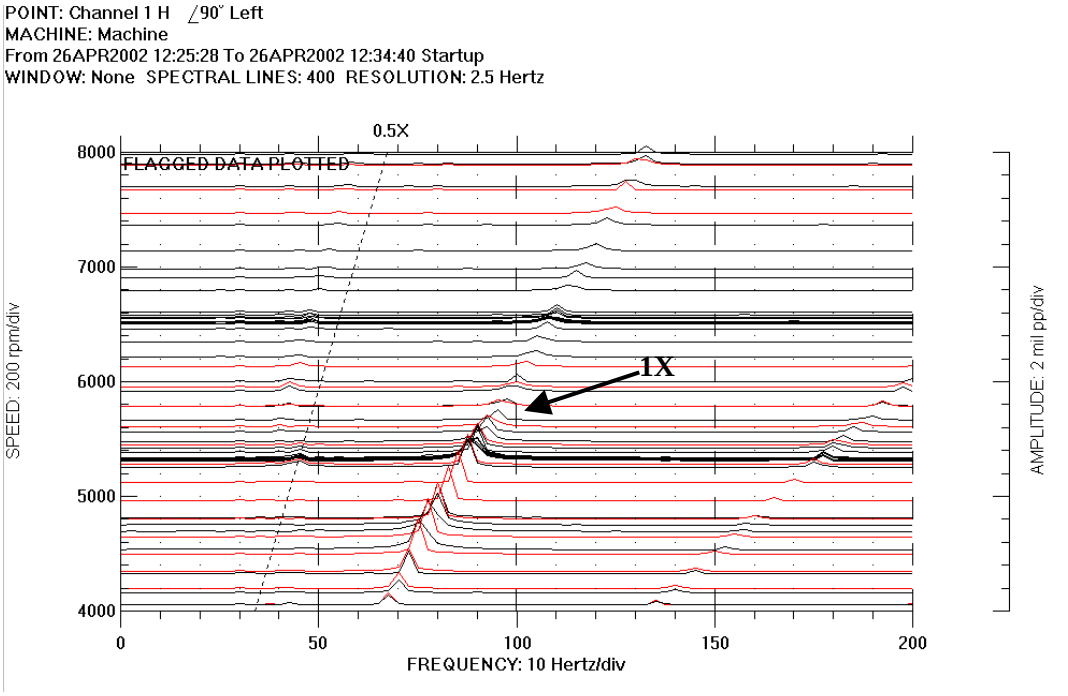

Figure 31: X probe cascade plot for tight fit without constraining foundation after tightening lock nut

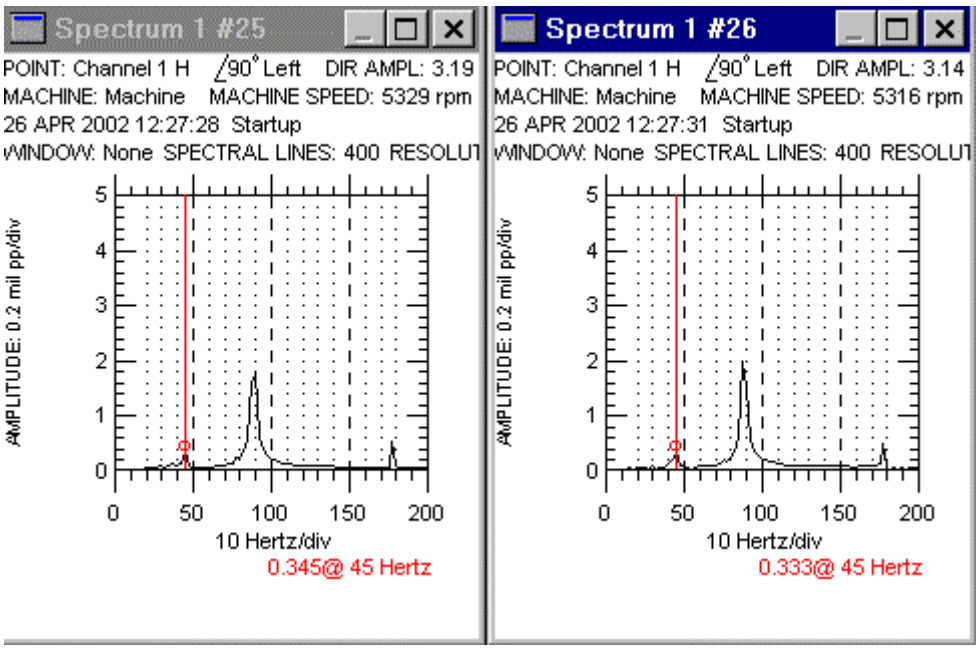

Figure 32: Frequency spectrum at 5300 rpm

Modeling using XLTRC2

The rotordynamic computer code XLTRC2 was used to model the response of the system and attempt to predict the onset speed of instability. The XLTRC model, created by Mir and Khalid [15], [16], was used as the basis and was converted to an XLTRC2 model using the XLTRC to XLTRC2 conversion feature in the software. The earlier researchers [15], [16], however, had used a single layered model in which they had determined the equivalent stiffness and damping parameters of the supports, assuming the bearing and the foundation to be in series. They had obtained the equivalent stiffness and damping using the XLFKCMHV™ sheet of XLTRC and had used this as the bearing file link in the code. This equivalent model is based on the assumption of synchronous whirl, while the frequency of interest in the problem is the subsynchronous frequency. Hence the equivalent model was not used in the analysis presented below.

A look at the bearing installation reveals that the shaft is supported by the bearing (which has the ball bearing stiffness), and this in turn is mounted on the foundation (which has its own damping and stiffness). The model is shown in Figure 33.

A 2-layer XLTRC2 model was constructed; the shaft was modeled with 24 stations. Layer 1 is the shaft and layer 2 is the foundation. The modal mass of the foundation was included as an added mass term in the model. The XLBALBRG™ spread sheet was used to get the ball bearing stiffness and damping values. The input parameters to the sheet are shown in Table 1. These bearing stiffness and damping values were entered in the XLUSEKCM™ chart (shown in Table 2) and were used as the internal bearing (to represent the stiffness and damping values of the element between the shaft and the ball bearings) in the model.

The foundation damping and modal mass measured by Xu [22] were input using a separate XLUSEKCM™ chart, and these were added as a constrained bearing (to represent the stiffness

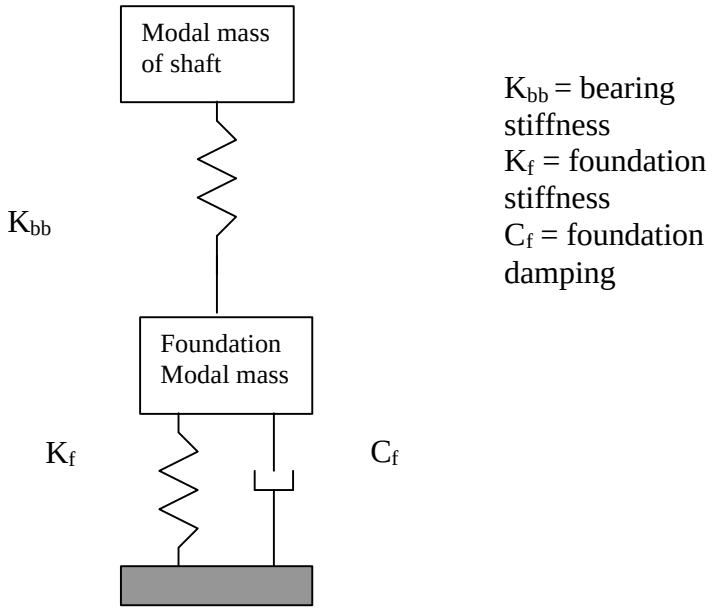

Figure 33: Model of the rotor-bearing system

and damping values of the element between the ball bearings and the foundation) in the model. This coupled stiffness, chosen in such a way (refer to appendix C) as to stabilize the rotor at speeds below the critical and destabilize at speeds above the critical speed.

Table 1 : Ball bearing spread sheet XLBALBRG

***XLBalBrg*™ Spreadsheet for Ball Bearing Stiffness**

Title: Shell Rotor ball brg details

Number of Balls	20	--	**Design Contact Angle β**	10	**degrees**
Ball Diameter	0.5	**inches**	**Internal Clearance (add to β)**	0	**inches**
Pitch Diameter	4.114	**inches**	**X Axis B.C.**	87.5	lbf
Outer Race Curvature	0.52	--	**Z Axis B.C.**	20	lbf
Inner Race Curvature	0.516	--	**Y Axis Deflection**	0	**inches**
O.R. Poisson's Ratio	0.25	--	**About X Axis Rotation**	0	**radians**
I.R. Poisson's Ratio	0.25	--	**About Y Axis Rotation**	0	**radians**
Ball Poisson's Ratio	0.25	--	**Outer Race Speed**	0	**rpm**
O.R. Elastic Modulus	2.90E+07	**psi**	**Inner Race Speed**		**rpm**
I.R. Elastic Modulus	2.90E+07	**psi**	**Ball Density**	0.283	**lb/in^3**
Ball Elastic Modulus	2.90E+07	**psi**			

Speed	Kxx	Kxy	Kyx	Kyy	Cxx	Cxy	Cyx	Cyy
rpm	lb/in	lb/in	lb/in	lb/in	lb-s/in	lb-s/in	lb-s/in	lb-s/in
0	5.68E+05	0.	0.	5.68E+05	3	0	0	3
2000	5.77E+05	0.	0.	5.77E+05	3	0	0	3
4000	5.37E+05	0.	0.	5.37E+05	3	0	0	3
6000	4.89E+05	0.	0.	4.89E+05	3	0	0	3
8000	4.54E+05	0.	0.	4.54E+05	3	0	0	3
10000	4.39E+05	0.	0.	4.39E+05	3	0	0	3

Table 2: Foundation parameters spread sheet XLUSEKCM

***XLUseKCM*™ User Defined Support Stiffness, Damping, and Mass Rotordynamic Coefficients** Press Control-F1 for help.

Title: Jiankang's values for foundation

Perform a Paste/Special/Link for the Title box within XLTRC to create a link to your rotor model.

Speed	Kxx	Kxy	Kyx	Kyy	Cxx	Cxy	Cyx	Cyy	Mxx	Mxy	Myx	Myy
rpm	lb/in	lb/in	lb/in	lb/in	lb-s/in	lb-s/in	lb-s/in	lb-s/in	lb-s**2/in	lb-s**2/in	lb-s**2/in	lb-s**2/in
1	95000	0	0	131000	60	0	0	190	0	0	0	0
2000	95000	0	0	131000	60	0	0	190	0	0	0	0
4000	95000	0	0	131000	60	0	0	190	0	0	0	0
6000	95000	0	0	131000	60	0	0	190	0	0	0	0
8000	95000	0	0	131000	60	0	0	190	0	0	0	0
10000	95000	0	0	131000	60	0	0	190	0	0	0	0

Table 3: Cross coupled stiffness terms sheet XLFKCMHV

XLUseKCM™ **User Defined Support Stiffness, Damping, and Mass R**

Version 2.0, Copyright 1996 - 1998 by Texas A&M University. All rights res

Title:	Damping Kxy and Kyx

Perform a Paste/Special/Link for the Title box within XLTRC to create a link to yc

Speed	Kxx	Kxy	Kyx	Kyy	Cxx	Cxy
rpm	lb/in	lb/in	lb/in	lb/in	lb-s/in	lb-s/in
1	0.	-1.	1.	0	0	0
185	0.	-116.	116.	0	0	0
369	0.	-232.	232.	0	0	0
554	0.	-348.	348.	0	0	0
738	0.	-464.	464.	0	0	0
923	0.	-580.	580.	0	0	0
1,108	0.	-696.	696.	0	0	0
1,292	0.	-812.	812.	0	0	0
1,477	0.	-928.	928.	0	0	0
1,662	0.	-1044.	1044.	0	0	0
1,846	0.	-1160.	1160.	0	0	0
2,031	0.	-1276.	1276.	0	0	0
2,215	0.	-1392.	1392.	0	0	0
2,400	0.	-1508.	1508.	0	0	0
2,585	0.	-1624.	1624.	0	0	0
2,769	0.	-1740.	1740.	0	0	0
2,954	0.	-1856.	1856.	0	0	0
3,138	0.	1972.	-1972.	0	0	0
3,323	0.	2088.	-2088.	0	0	0
3,508	0.	2204.	-2204.	0	0	0
3,692	0.	2320.	-2320.	0	0	0
3,877	0.	2436.	-2436.	0	0	0

The magnitude of the internal friction was adjusted until it closely predicted the threshold speed of instability for the case without stiffening the foundation. This value turned out to be 6 lb-s/in. The sheet used for the cross-coupled stiffness terms is shown in Table 3.

In summary, the two-layered model was constructed with the shaft as the first layer and the foundation as the second layer. The foundation mass was added as an inertia term to the second layer, and this second layer was made non-rotating (the rotation value in the model sheet of XLTRC2 was 0). The geo plot of the model is shown in Figure 34.

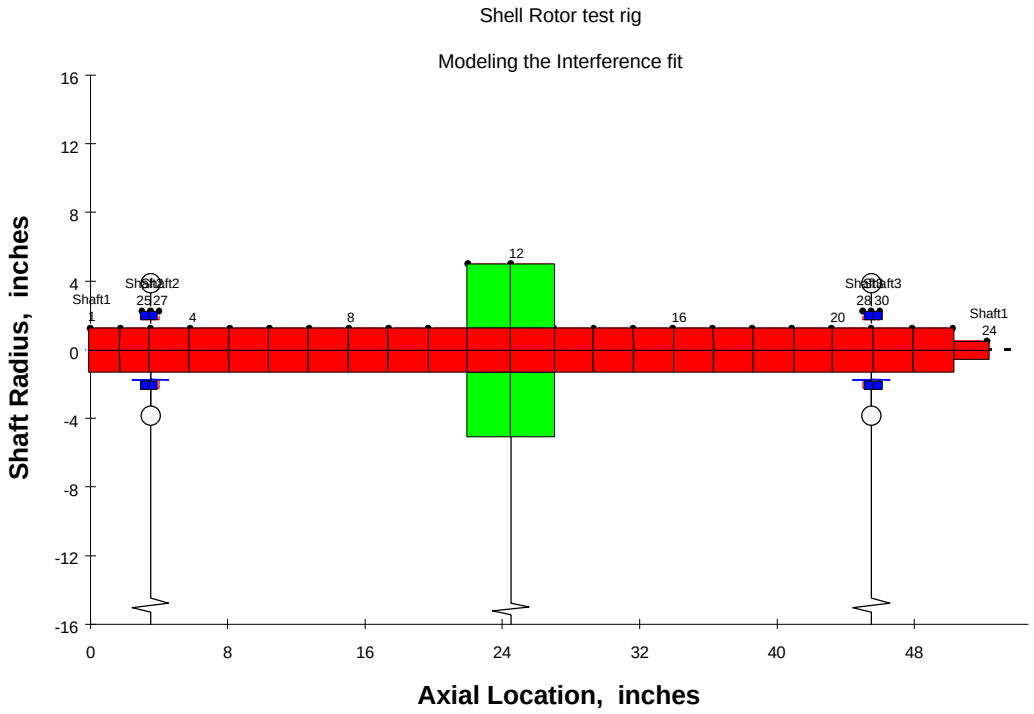

Figure 34: Geo plot of the rotor

The foundation modal mass and the stiffness were varied to match the horizontal and the vertical direction Bode plot results of the model without the cross-coupled stiffness terms. The matched results are shown in Figure 35, 36.

The eigenvalue analysis of XLTRC2 predicts that the rotor goes unstable at 7385 rpm (Table 4). The running tests reveal instability at speed close to 7100 rpm. The stiffness along the horizontal axis was increased (the value of K_{xx} in the foundation parameters was increased) and, the model then predicts that the rotor will become unstable at 5169 rpm. This instability is shown in Table 5, and was observed in the experiments done both with the foundation stiffened horizontally and with tight and loose fits.

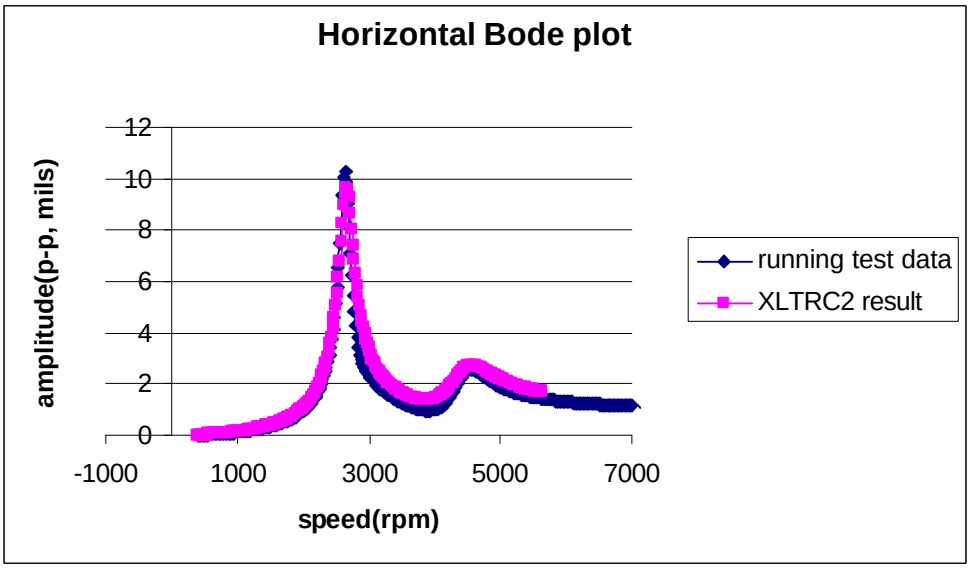

Figure 35: Horizontal Bode plot matched for base case

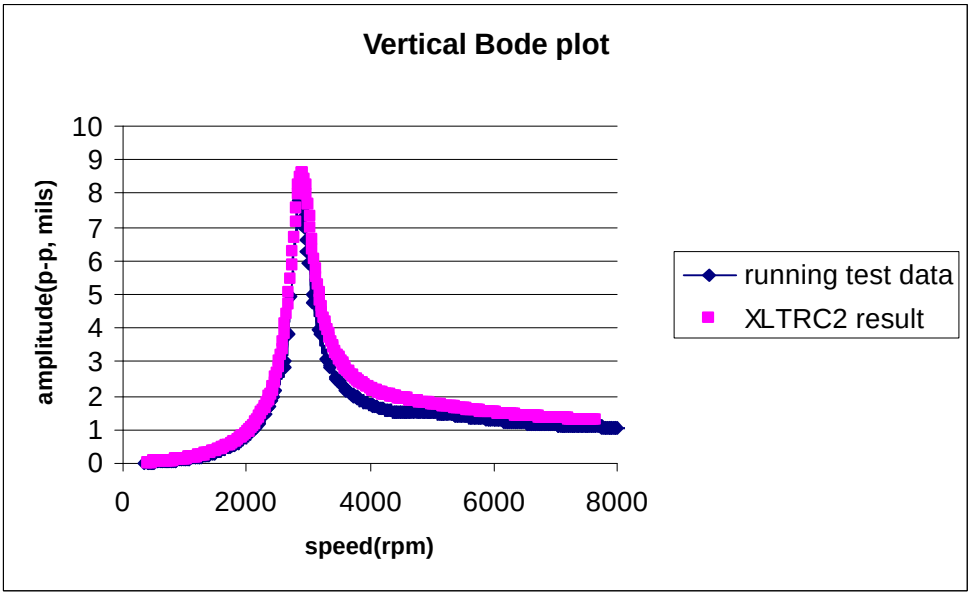

Figure 36: Vertical Bode plot matched for base case

Table 4: Damped roots showing onset speed of instability at 7385 rpm

Speed	zeta1	cpm1	zeta2	cpm2	zeta3
5169.	0.000	9.7	0.035	2723.1	0.063
5354.	0.000	9.7	0.033	2732.2	0.066
5538.	0.000	9.7	0.030	2740.9	0.068
5723.	0.000	9.7	0.027	2748.2	0.072
5908.	0.000	9.7	0.023	2754.1	0.075
6092.	0.000	9.7	0.020	2758.7	0.079
6277.	0.000	9.7	0.016	2762.4	0.082
6462.	0.000	9.7	0.013	2765.6	0.085
6646.	0.000	9.7	0.010	2768.3	0.088
6831.	0.000	9.7	0.007	2770.7	0.091
7015.	0.000	9.7	0.004	2772.8	0.094
7200.	0.000	9.7	0.001	2774.8	0.097
7385.	0.000	9.7	**-0.002**	**2776.7**	0.100
7569.	0.000	9.7	-0.005	2778.5	0.102
7754.	0.000	9.7	-0.008	2780.2	0.105
7938.	0.000	9.7	-0.010	2781.9	0.108
8123.	0.000	9.7	-0.013	2783.5	0.110
8308.	0.000	9.7	-0.016	2785.2	0.113

Table 5: Damped roots showing instability at 5169 rpm with horizontal foundation stiffness increased

Speed	zeta1	cpm1	zeta2	cpm2	zeta3
3323.	0.000	9.7	0.016	2835.7	0.064
3508.	0.000	9.7	0.014	2837.6	0.065
3692.	0.000	9.7	0.013	2839.5	0.067
3877.	0.000	9.7	0.011	2841.3	0.068
4062.	0.000	9.7	0.009	2843.0	0.070
4246.	0.000	9.7	0.008	2844.6	0.072
4431.	0.000	9.7	0.006	2846.2	0.074
4615.	0.000	9.7	0.004	2847.6	0.076
4800.	0.000	9.7	0.002	2848.9	0.078
4985.	0.000	9.7	0.000	2850.2	0.080
5169.	0.000	9.7	**-0.002**	**2851.4**	0.082
5354.	0.000	9.7	-0.005	2852.5	0.084
5538.	0.000	9.7	-0.007	2853.6	0.086
5723.	0.000	9.7	-0.009	2854.6	0.088
5908.	0.000	9.7	-0.011	2855.6	0.090
6092.	0.000	9.7	-0.013	2856.6	0.092

Discussion of results

An attempt was first made to understand the subsynchronous whirl of the base case as the destabilizing effect of internal friction. The stiffness of the foundation was increased along the horizontal direction to make it more symmetrically stiff along the x and the y directions. The data then shows no instability without a balance mass. This contradicts the theory [5] that predicts a stabilizing effect of support stiffness asymmetry. However, the addition of a balance screw produced large subsynchronous signatures with the frequency slightly higher than 0.45 times the running speed. This contradicts the theory [8] that predicts no effect of unbalance.

Most of the subsynchronous peaks occurred over a very small range of the running speed. Hence, the runup and coastdown data are not an ideal way to capture these subsynchronous peaks. Tests done by hovering the machine around the speed of 5500 rpm revealed more useful results.

The tests show that subsynchronous frequencies occurred in the range of 5500-5700 rpm irrespective of the tightness of the fit (between the sleeve and the disk) and the stiffness of the foundation. The large subsynchronous amplitude appeared only after balancing the rotor. The drive belt was constrained, thus eliminating its possible effect on the vibration signature. After locating a loose lock nut in the bearing as a cause of the high subsynchronous vibrations, the tests were repeated. The data are presented in Figures 28 through 32. The largest amplitude subsynchronous vibration peaks that appeared in Figures 13,18,19,20,21 disappear after the bearing lock nut is tightened. The subsynchronous frequencies that remain are also seen to be different. Lin [23] reports subsynchronous vibrations induced by radial clearances in ball bearing supports. However subsynchronous vibration due to a loose ball bearing is from an externally applied forcing function on the system and does not drive the system unstable (the orbit is bounded). Internal friction produces a follower force that supplies energy to the system, and the orbit grows exponentially before catastrophic failures could occur [24].

The “Fundamental Train Frequency” [24] created due to the rotation of the ball bearing cage is given by

$$FTF = \frac{1}{2}\frac{rpm}{60}\left(1-\frac{Bd}{Pd}\cos b_b\right) \qquad \textbf{Eq 3. 5}$$

where

Bd	=	Ball diameter
Pd	=	Pitch diameter
b_b	=	Contact angle
$\frac{rpm}{60}$	=	N = rotor speed (rev/s)

For the ball bearings used, the values are Pd = 104.50 mm (4.114”), Bd = 12.7 mm (0.5”), and the contact angle b_b = 10^o. Substituting these values in the above equation, we get the FTF to be 0.44 times the running speed.

The data show two speed ranges where subsynchronous frequencies occur, one at speeds close to 5200 rpm and the other at 6200 rpm. It can be seen that the subsynchronous frequency at 5200 rpm is close to 0.5 times the running speed, and the one at 6200 rpm is around 0.43 times the running speed. A small 30 Hz frequency subsynchronous vibration is also observed in the data. An accelerometer was mounted on the oil pump and indicated a frequency of 30 Hz. Hence the 30 Hz frequency in the running test data is due to the oil pump vibrations transmitted to the foundation through the lubrication line that connects the outlet of the bearing to the oil sump.

It is believed that the 0.43X frequency may be due to the fundamental train frequency of the ball bearings excited at that speed range. One way to determine if the vibration is benign or harmful may be to look at the filtered orbit at the fractional speed. However, the Nx vector in ADRE has to be specified before the tests are started. Thus, one has to guess beforehand the value of the subsynchronous frequency. One can increment the Nx vector only in steps of 0.025, so that only the 0.5X orbits can be filtered.

The filtered orbits of the 0.5X frequency are predominantly circular (see Figure 29), hence could be a possible indication of an instability due to internal friction. Murphy [21] showed that circular orbits are more prone to instability, since the tangential follower force that tends to drive the system unstable remains perpendicular to the rotor displacement vector at all times (in the

same direction of the orbit velocity). However, the test data revealed subsynchronous frequencies even with a tight fit (no internal friction). The data collected for the tight fit without constraining the foundation (more asymmetry) reveal no large subsynchronous amplitudes, and the 0.5X filtered orbits are elliptical.

These experiments suggest that subsynchronous vibration in rotating machinery can have numerous sources or causes. Also the subsynchronous whirl due to internal friction is not a highly repeatable phenomenon. The tests show subsynchronous frequencies only during the coastdown, possibly due to the wheel becoming loose. The subsynchronous vibration depends on the state of rotor balance. Subsynchronous vibrations can be produced by ball bearing dynamics, a loose ball bearing or excitation from a nearby machine; therefore subsynchronous signatures may not necessarily indicate instability.

CHAPTER VI

QUANTIFYING INTERNAL FRICTION

One of the problems associated with internal friction is the lack of numbers to characterize it. Experiments at the laboratory have shown that the subsynchronous component due to internal friction is not repeatable, and does not appear in all tests.

Mir [16] and Khalid [15] had done experiments with the taper-sleeve arrangement, but were unable to produce enough friction to consistently drive the system unstable. Further, the threshold speed was close to the maximum operating speed of the machine, making it difficult to perform satisfactory tests. Bently and Muszynska [11] give a method of increasing the internal friction by adding damping material in the form of a tape on the shaft. A self bonding (no glue) tape was wrapped on both sides of the disk on our shaft in order to increase the internal friction. By doing so, the threshold speed of instability was brought down to an analyzable speed. Runup and coastdown tests were conducted on the rotor. This chapter summarizes the results both with and without the self-bonding tape and both with and without the disk on the shaft.

Running tests

Runup and coastdown tests were done on the system for both high and low interference fits with the tape and the results are shown in Figure 37 and 38. It can be seen that the onset speed of instability is around 5500 rpm, much lower than for the tests done without the tape.

The same types of signatures were noted for both tight and loose fits of the disk. Hence it can be argued that the subsynchronous frequency is due to the addition of the tape on the shaft. To confirm this conclusion, the next step was to study the characteristics of the internal friction induced by the tape. For this study the shaft was hung free-free and non-rotating tests were conducted to determine the amount of internal damping.

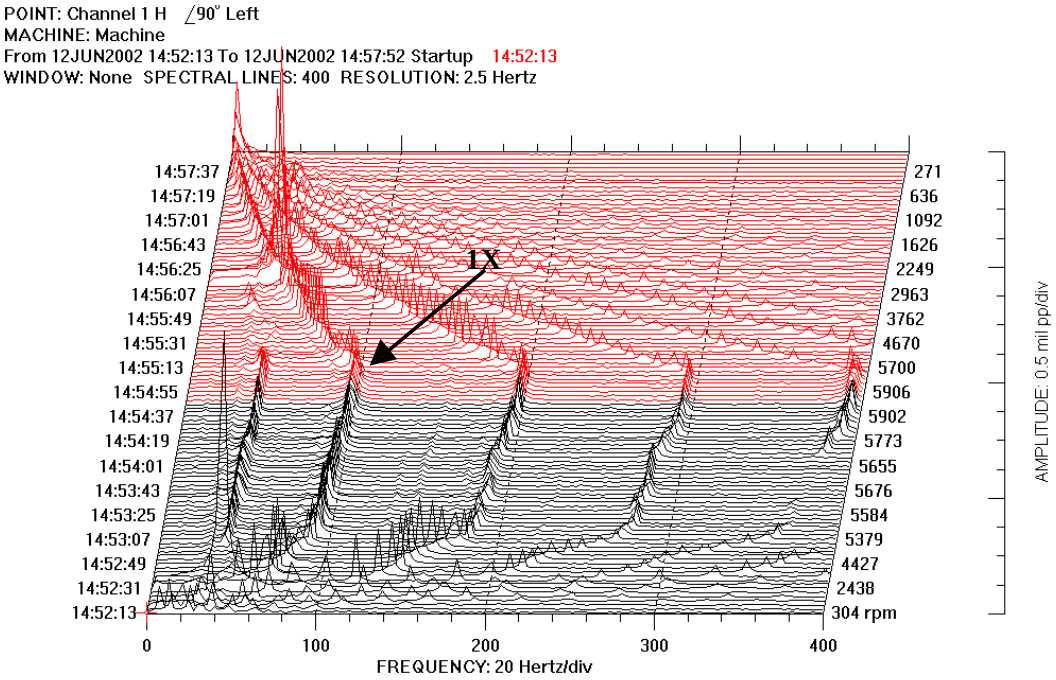

Figure 37: Waterfall plot for the system with tape, low interference

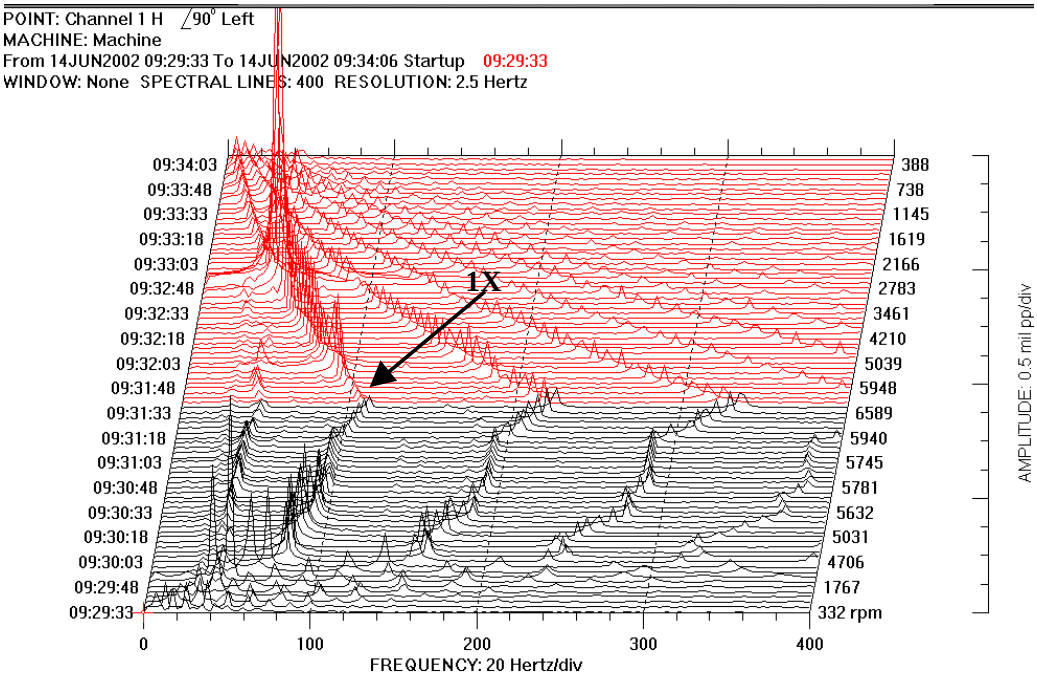

Figure 38: Waterfall plot for the system with tape, high interference

Free vibration tests

Mir [16] and Khalid [15] conducted rap tests by hanging the rotor free-free and determined the logarithmic decrement of the system. However, one of the concerns of a rap test is to simulate the running speed peak amplitude, and the only way of doing this is to rap the rotor hard enough so that the peak amplitude due to the impulsive force of the hammer is comparable with the running speed peak amplitude.

Shaker tests

In order to simulate the running speed amplitudes in a static test, a shaker test on the rotor was designed and carried out. The shaker, being capable of exerting about 14 kg (30-lb) force over a range of frequencies, was a good alternative to the rap tests. The forcing function can be used to get a transfer function of the displacement to the applied force, from which the parameters can be extracted.

The disk-shaft system

Modeling the disk-shaft system

The rotor has most of its mass concentrated at the disk; applying a shaker force at the disk will cause it to displace through a distance smaller than the ends of the shaft. The ends of the shaft act as the ends of a cantilevered beam with the fixed end at the disk. Thus a periodic forcing function at the disk will cause the center and the ends to vibrate out of phase and with different amplitudes, the ends with bigger amplitude compared to the center. Hence a 2 degree of freedom model was used. The disk-shaft system, with the relative displacements when hung free-free and shaken at the disk, is shown in Figure 39.

This system can be modeled as shown on the left hand side of Figure 40. The 2 DOF system is converted to an equivalent single DOF system (represented on the right hand side of Figure 40), with the equivalent displacement given by

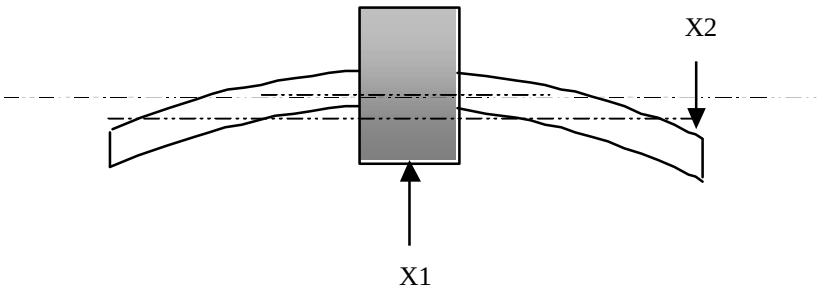

Figure 39: Motion of the disk-shaft system when hung free-free

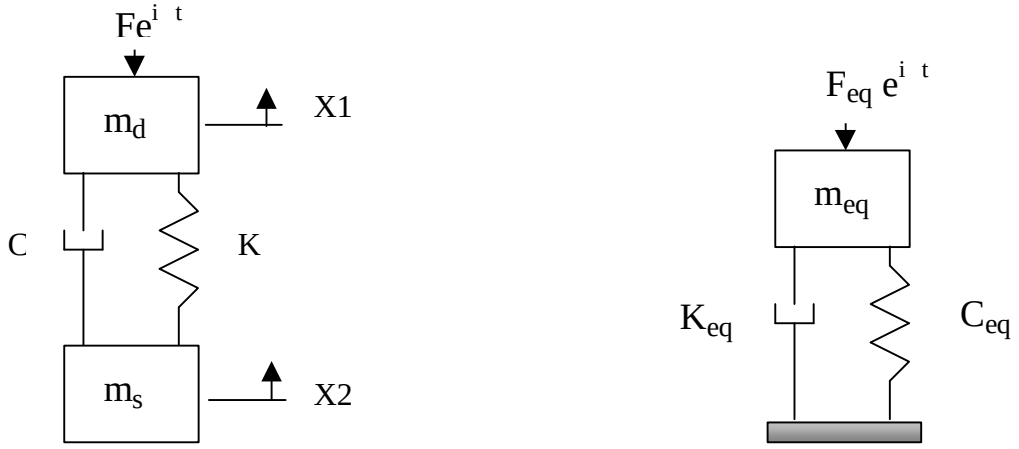

Figure 40: 2 DOF model of disk-shaft system and the equivalent 1 DOF model

$$X_{eq} = X_1 - X_2 \qquad \textbf{Eq 6. 1}$$

The equations of motion for the 2 DOF system are:

$$m_d \ddot{X}_1 + C(\dot{X}_1 - \dot{X}_2) + K(X_1 - X_2) = Fe^{iwt} \qquad \textbf{Eq 6. 2}$$

$$m_s \ddot{X}_2 + C(\dot{X}_1 - \dot{X}_2) + K(X_1 - X_2) = 0 \qquad \textbf{Eq 6. 3}$$

Dividing Equation 6.2 and Equation 6.3 by m_d and m_s respectively, and subtracting the resulting equations, we get

$$(\ddot{X}_1 - \ddot{X}_2) + K\left[\frac{1}{m_d} + \frac{1}{m_s}\right](X_1 - X_2) + C\left[\frac{1}{m_d} + \frac{1}{m_s}\right](\dot{X}_1 - \dot{X}_2) = \frac{F}{m_d}e^{iwt} \qquad \textbf{Eq 6. 4}$$

Let $(X_1 - X_2) = X_{eq}$. Then Equation 6.4 becomes

$$(\ddot{X}_{eq}) + K\left[\frac{1}{m_d} + \frac{1}{m_s}\right](X_{eq}) + C\left[\frac{1}{m_d} + \frac{1}{m_s}\right](\dot{X}_{eq}) = \frac{F}{m_d}e^{iwt} \qquad \textbf{Eq 6. 5}$$

The equivalent single degree of freedom equation is given by

$$m_{eq}\ddot{X}_{eq} + C_{eq}\dot{X}_{eq} + K_{eq}X_{eq} = F_{eq}e^{iwt} \qquad \textbf{Eq 6. 6}$$

Comparing equation 6.5 and equation 6.6 we get

$$M_{eq} = \frac{m_d\, m_s}{m_d + m_s} \qquad \textbf{Eq 6. 7}$$

$$K_{eq} = K \qquad \textbf{Eq 6. 8}$$

$$C_{eq} = C \qquad \textbf{Eq 6. 9}$$

$$F_{eq} = \frac{F\, m_s}{m_d + m_s} \qquad \textbf{Eq 6. 10}$$

The transfer function for the equivalent system is given by

$$\frac{X_{eq}}{F_{eq}} = \frac{1}{(K_{eq} - M_{eq}\, w^2) + i\, C_{eq}\, w} \qquad \textbf{Eq 6. 11}$$

Thus the magnitude and phase of the transfer function of the original system can be written as

$$\left|\frac{X_1 - X_2}{F}\right| = \frac{\dfrac{m_s}{m_d + m_s}}{\sqrt{\left[K - \dfrac{m_s\, m_d}{m_s + m_d} w^2\right]^2 + \left[C\, w\right]^2}} \qquad \textbf{Eq 6. 12}$$

$$f = \tan^{-1}\left(\frac{C\, w}{K - \dfrac{m_s\, m_d}{m_s + m_d} w^2}\right) \qquad \textbf{Eq 6. 13}$$

Determination of the disk (m_d) and the shaft (m_s) masses

The disk, being a heavy mass concentrated at the center, moves a smaller distance due to the force compared to the ends of the shaft. Since the disk as a whole and a part of the shaft mass participate in the motion, the mass of the disk m_d that participates in the motion can be estimated to be 110% of the disk mass.

$$\therefore\ m_d = 1.1 \times 45.45 = 50 \text{ kg (110 lb)}$$

The shaft is a cantilevered beam, with the ends tending to move in a direction opposite to the applied force. For a cantilevered beam, the equivalent modal mass is 33/140 times the shaft mass [17]. In this case, the shaft hangs on either side of the disk. Hence the mass of the shaft to be considered will be twice the value of the shaft mass on one side multiplied by the fraction.

$$\therefore\ m_s = \frac{33}{140} \times 17.05 \times 2 = 8.04 \text{ kg (18 lb)}$$

Determination of modal mass

The equivalent modal mass from equation 6.7 is 7.03 kg (15.47 lb).

The modal mass was also determined from the XLTRC2 model. The normalized zero speed mode shape was determined and from the mass of each element, the modal mass was determined from the equation

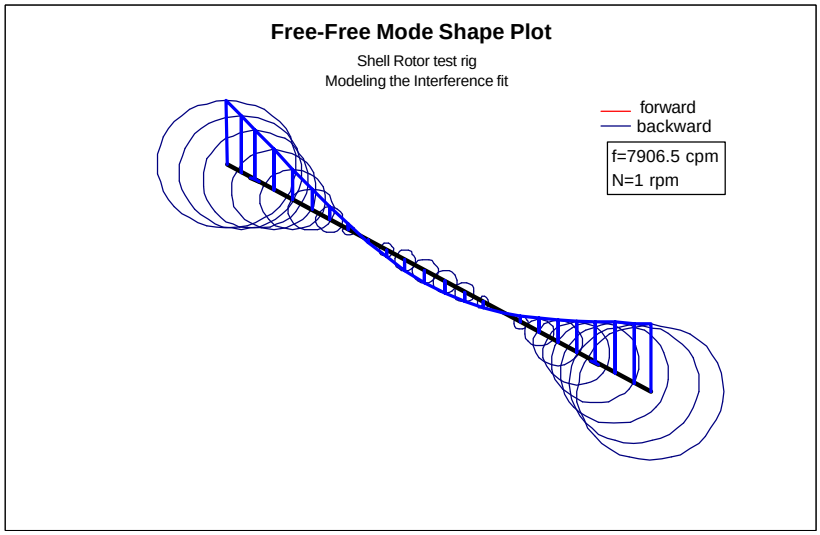

Figure 41: Mode shape of the disk-shaft system

$$M_{eq} = \sum m_i Z_i^2 \qquad \textbf{Eq 6. 14}$$

where m_i is the mass of each element in the model and Z_i is the normalized displacements at each location. From Eqn 6.14, the modal mass was obtained as 6.85 kg (15.08 lb). Figure 41 shows the normalized mode shape.

Determination of modal stiffness

Since the shaft is assumed to be cantilevered, the modal stiffness, accounting for both the ends vibrating could be approximated by

$$K_{eq(di)} = \frac{3EI}{L^3} \cdot 2 \qquad \textbf{Eq 6. 15}$$

where E is the Young's modulus of the material ($E = 206.8$ GPa [30 E+6 lb/in^2]), I is the moment of inertia about the transverse axis of the shaft ($I = \frac{p}{64} d^4$ =7.98x10^5 mm^4 [1.917 in^4])

and L is the length of the shaft ($L = 597$ mm [23.5 in]). Substituting these values, K is obtained as 4.659 MN/m (26594.93 lb/in). The natural frequency is then given by

$$w_{n(di)} = \sqrt{\frac{K_{eq(di)}}{M_{eq(di)}}} = \frac{1}{2p}\sqrt{\frac{26594.93}{\frac{18\times110}{128}\times\frac{1}{386.4}}}$$

$$w_{n(di)} = 129.72 \text{ Hz}$$

The measured undamped natural frequency was actually between 124 and 128 Hz depending on the tightness of the fit. During the subsequent analysis, the equivalent stiffness was obtained from the relation

$$K_{eq} = M_{eq}\, w_n^2 \qquad \textbf{Eq 6. 16}$$

Determination of internal damping

Once the transfer function data were obtained experimentally, Eqns 6.11 and 6.12 were used to plot the magnitude and phase of the transfer function. The 90-degree phase shift method was used to get the damping value. The damping at the 90-degree phase is given by

$$C_{90} = \frac{1}{M_{90}\, w_{90}} \qquad \textbf{Eq 6. 17}$$

where M_{90} = magnitude at a phase of 90^0

w_{90} = frequency at phase of 90^0

The arrangement for the shaker test is shown in Figure 42. The rotor was hung free-free to eliminate all other sources of external damping. A steel piece was bolted to the disk, which in turn was used to attach the force transducer and the shaker. The periodic chirp signal with a frequency range of 0-200 Hz was used to excite the shaft. The Ling Dynamic Systems 400 series shaker was used. Two accelerometers were mounted, one on the disk and the other on one end of the shaft. The voltage signals from the accelerometers and the force transducer were collected using a custom-made virtual instrument in LabVIEW. A Mathcad code was written to analyze the data obtained from the tests.

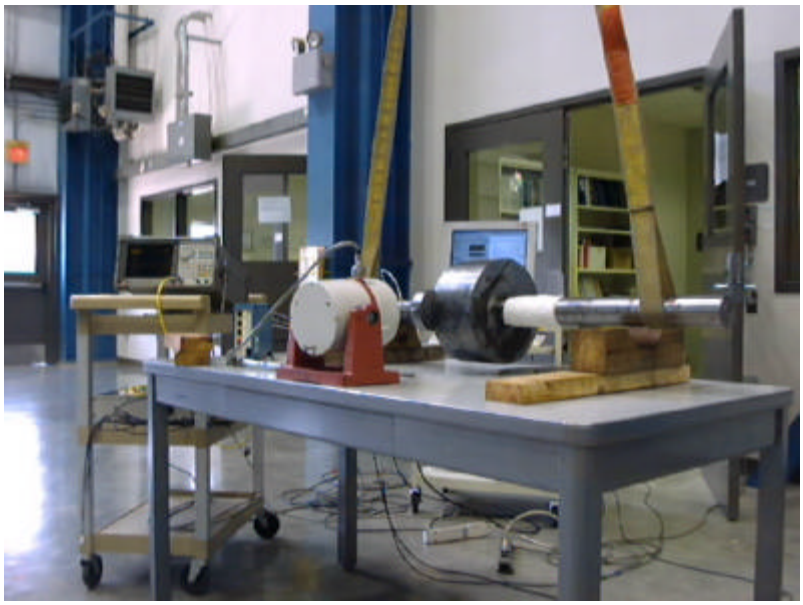

Figure 42: Set-up arrangement

Analysis technique

The voltage data from the accelerometers and the force transducer were acquired using LabVIEW. The frequency range and the resolution of the spectrum plots depend on the sampling rate and the number of points acquired. The frequency span used in the shaker was 200 Hz, starting from 0 Hz. To get a resolution of 0.5 Hz on the free spectrum, the number of points and the sampling rate calculated were as follows:

The frequency resolution is related to the sampling rate (F_s) and the number of samples (N) by

$$\Delta f = \frac{F_s}{N} \qquad \textbf{Eq 6. 18}$$

Alternatively, Δf can be expressed as

$$\Delta f = \frac{1}{N\,\Delta t} \qquad \textbf{Eq 6. 19}$$

where Δt is the sampling period.

The shaker takes about two seconds (determined by the spectrum analyzer, which supplies the frequencies to the shaker) to scan all frequencies from 0 to 200 Hz. If we acquire, say, 4096 samples, then

$$\Delta t = \frac{2}{4096}\ s \qquad \textbf{Eq 6. 20(a)}$$

From Eqn 6.18 we have

$$0.5 = \frac{F_s}{4096} \qquad \textbf{Eq 6.20(b)}$$

Hence the sampling rate was fixed at 2048 samples/s and 4096 points were gathered.
The following algorithm was used in Mathcad to analyze the data:

1. Acquire the time domain data points from the 2 accelerometers (manufactured by PCB) and the force transducer (manufactured by PCB) with LabVIEW. (Units = V)
2. Convert the data to the required Engineering units using the sensitivities of the accelerometer and the force transducer. The acceleration is now expressed in in/s^2 and force in lb.
3. Convert the time domain data to the frequency domain using the FFT function in Mathcad.
4. Get the transfer function $(a1 - a2)/F$ and convert that to $(X1 - X2)/F$ by dividing it by the square of the frequency at each frequency. (Units = in/lb)
5. Plot the magnitude and the phase of the transfer function and determine the damping from equation 6.17 by interpolating the magnitude for the 90-degree phase.

In addition to the above-calculated values, the curve-fitting algorithm in Mathcad was also used to get a set of values for the equivalent mass, stiffness and the internal damping. Thus 2 curves were generated using equations 6.12 and 6.13: one set with the calculated values of the modal parameters and the other with the values from the Mathcad curve-fit algorithm. These were compared with the experimental curve.

Results for the disk-shaft system without tape

The tests were done for both low and high interference fits. It was found that the damping for the low interference fit was higher than for the high interference. This is due to the fact that when

the fit is tight, slipping at the interference between the disk and the shaft is reduced. Mir [16] had predicted that the amount of damping in this system is amplitude dependent. An extract from his thesis is shown in Table 6. The shaker test results are shown in Table 7.

The damping values obtained from the shaker tests can be converted to a logarithmic decrement using the relation

$$d = \frac{p\ c_i}{M_{eq(si)}\ w_n} \qquad \textbf{Eq 6.21(a)}$$

Substituting the values for $M_{eq(di)}$ and w_n obtained from the theoretical calculations, we get

$$d = \frac{p \cdot c_i}{(0.0431) \cdot (125 \cdot 2 \cdot p)} \qquad \textbf{Eq 6.21(b)}$$

From Table 1, the value for the damping without the tape varies between 0.23 and 0.13 lb-s/in (40.64 and 22.94 N-s/m) depending on the tightness of the fit. Substituting these values in the above equation, the logarithmic decrement values are found to be between 0.021 and 0.012 for

Table 6: Extract from Mir's thesis showing the logarithmic decrement values of the free-free tests

Intere-rence [mm (mils)]	First Group (Data point)	Amp-litude	Log -dec	Second Group (Data point)	Ampli -tude	Log -dec	Third Group (Data point)	Ampli -tude	Log -dec	Fourth Group (Data point)	Ampli-tude	Log -dec
0.00241 (0.095)	1 to 2	0.28 to 0.12	0.346	3 to 7	0.11 to 0.077	0.051	8 to 12	0.021 to 0.016	0.0612	15 to 21	0.026 To 0.164	0.07
0.01067 (0.42)	1 to 2	0.23 to 0.11	0.32	3 to 6	0.099 to 0.08	0.03	7 to 25	0.078 to 0.027	0.0197	N/A	N/A	N/A
0.01572 (0.619)	1 to 2	0.41 to 0.18	0.345	3 to 7	0.167 to 0.124	0.031	6 to 14	0.133 to 0.079	0.0279	15 rest	0.075 to 0.035	0.02
0.02108 (0.83)	1 to 2	0.27 to 0.13	0.313	3 to 5	0.124 to 0.108	0.029	5 to 10	0.108 to 0.081	0.0243	8 to 24	0.092 to 0.031	0.02
0.02395 (0.943)	1 to 2	0.21 to 0.10	0.285	3 to 12	0.103 to 0.056	0.029	22 to 31	0.029 to 0.018	0.024	N/A	N/A	N/A
0.03098 (1.22)	1 to 2	0.25 to 0.16	0.193	3 to 6	0.145 to 0.117	0.032	9 to 14	0.081 to 0.059	0.0273	15 rest	0.058 to 0.011	0.02

small and large interference fits, respectively. These values are in the same range of the values as those determined by Mir for certain amplitudes and interference fits.

Results for the disk-shaft system with tape

To investigate the change in the damping due to the tape on the shaft, shaker tests were done both with and without the tape. The results are shown in Table 1. Figure 43 through 46 show the curve fits obtained by the two methods mentioned above. A comparison of the damping values is shown in Figure 47. It can be seen that the damping increases with the addition of the tape.

Table 7: Modal parameters for disk-shaft system with standard stinger

	Method used	**Stiffness lb/in (N/m)**		**Mass lb-s^2/in (kg)**		**Damping lb-s/in (N-s/m)**	
Type of fit		**Loose**	**Tight**	**Loose**	**Tight**	**Loose**	**Tight**
Without tape	90-degree damping (average)	NA	NA	NA	NA	0.2319 (40.64)	0.1559 (27.32)
	Curve fit for theoretical equations	25551.16 (4.47E6)	27462.87 (4.81E6)	0.0431 (7.57)	0.0431 (7.57)	0.2319 (40.64)	0.1559 (27.32)
	Curve fit From Mathcad algorithm (average)	19383.74 (3.39E6)	29753.74 (5.21E6)	0.0326 (5.74)	0.0468 (8.22)	0.2154 (37.74)	0.1309 (22.94)
With tape	90-degree damping (average)	NA	NA	NA	NA	0.3204 (56.15)	0.1958 (34.32)
	Curve fit for theoretical equations	25551.16 (4.47E6)	27462.87 (4.81E6)	0.0431 (7.57)	0.0431 (7.57)	0.3204 (56.15)	0.1958 (34.32)
	Curve fit From Mathcad algorithm (average)	18005.67 (3.15E6)	22291.89 (3.91E6)	0.0304 (5.34)	0.0352 (6.19)	0.3113 (54.54)	0.1883 (33.00)

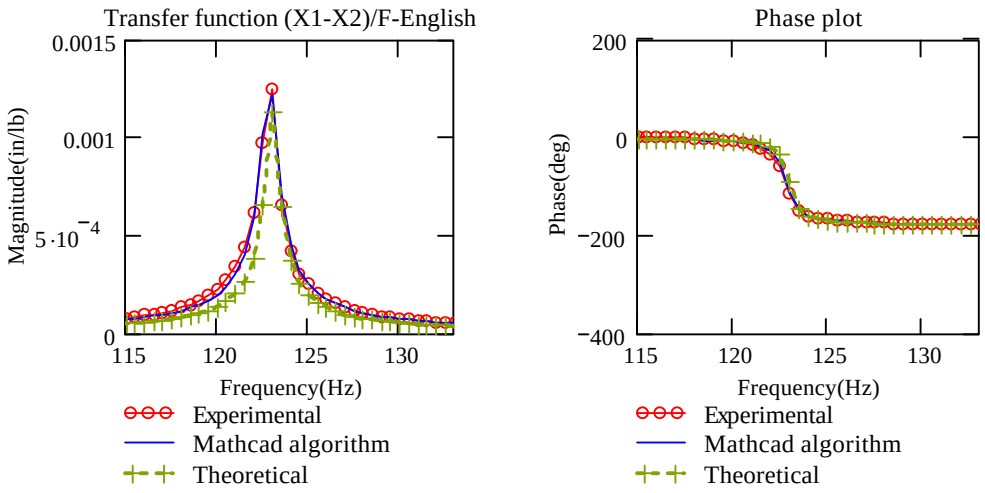

Figure 43: Loose fit with tape on both sides

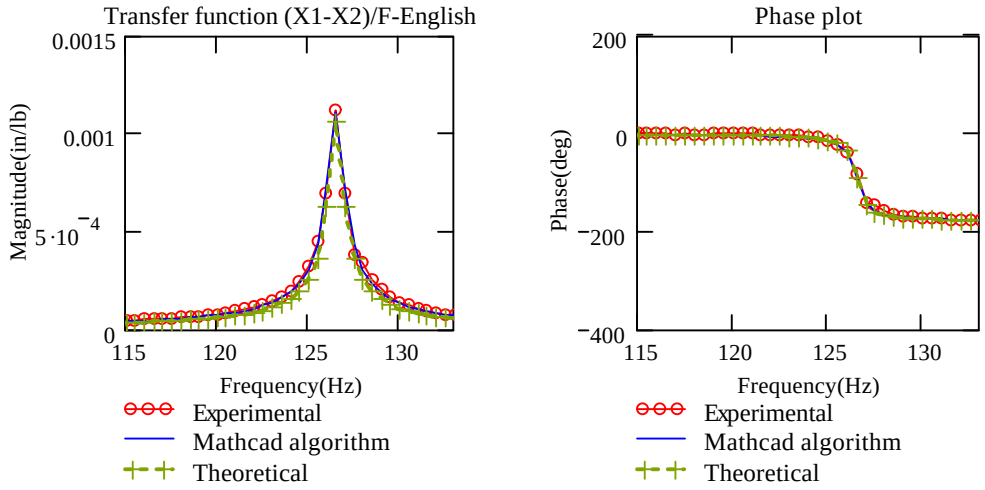

Figure 44: Tight fit with tape on both sides

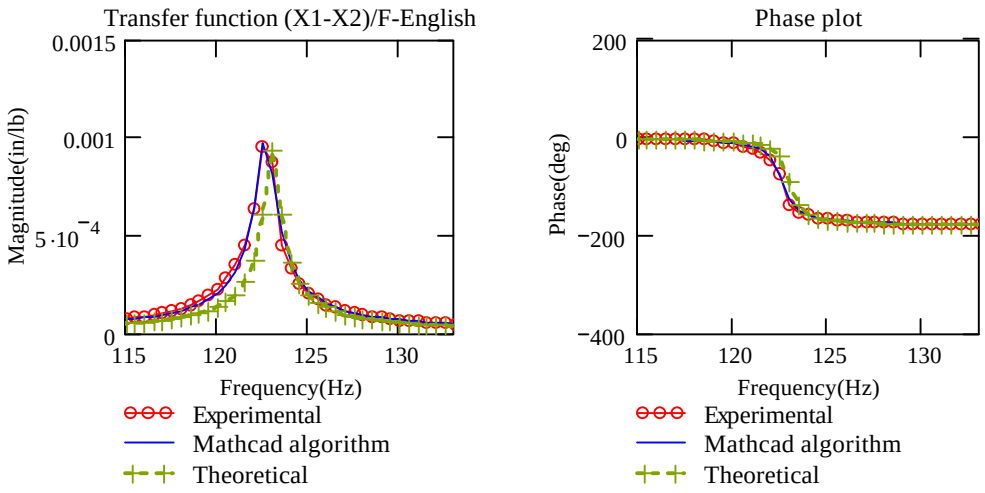

Figure 45: Loose fit with no tape

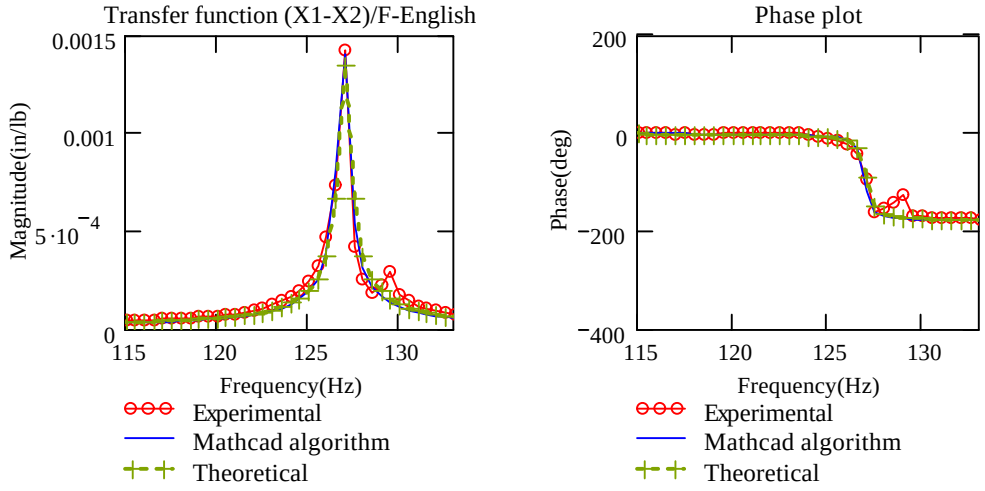

Figure 46: Tight fit with no tape

To verify the validity of the Mathcad graphs, the algorithm was written as a virtual instrument in LabVIEW. The VI was used to compare the peak values of the curves plotted in Mathcad and in

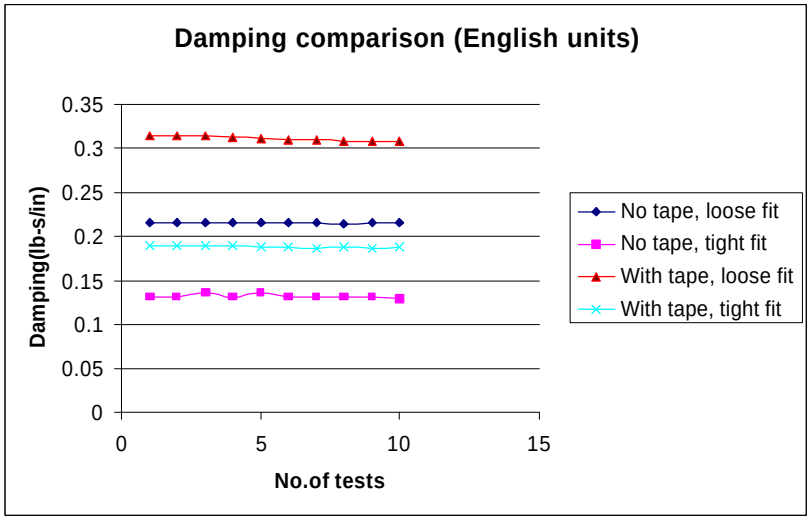

Figure 47: Damping comparison for 90 degree method

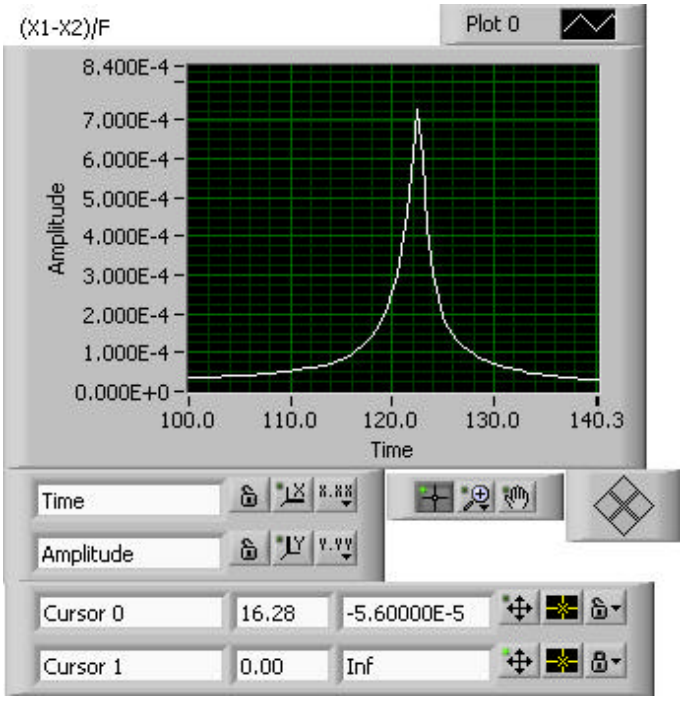

Figure 48: LabVIEW verification

LabVIEW. The graph for the case of the disk on the shaft with tape on both sides and with a low interference fit is shown as a LabVIEW result in Figure 48.

Modeling of the disk-shaft system using XLTRC2

The free-free rotor assembly was modeled in XLTRC2 with the same two-layered 24-station model and with cross-coupled stiffness terms to include the effect of damping as described in Chapter 5. The coefficients obtained from the shaker tests are modal parameters. The damping value C_i obtained in these tests above is the modal damping. The actual system damping is different from the modal damping. The modal damping is related to the damping ratio of the system according to Eqn 6.22.

$$x = \frac{C_{Modal}}{2 \cdot M_{eq}\, w_{n(di)}} = \frac{C_i}{2 \cdot M_{eq}\, w_{n(di)}} \qquad \textbf{Eq 6.22}$$

From Eqn 6.22, the damping ratio for the disk-shaft system with tape varies between 0.00509 and 0.00313, depending on the tightness of the fit.

The actual damping in the system is determined in XLTRC2 as follows: the internal damping in the system is represented as cross-coupled stiffness coefficients at the location of the disk. These coefficients are calculated [24] using the relation

$$K_{XY} = -K_{YX} = C\, w_n \qquad \textbf{Eq 6.23}$$

where w_n is the resonant frequency in the free-free test. The damping ratios to simulate the free-free case were determined by running the damped eigenvalue case in XLTRC2 with zero stiffness coefficients for the bearings. The value of the damping coefficient used in the cross-coupled stiffness terms in Eqn 6.23 was varied until the damping ratio in XLTRC2 matched the value calculated from Eqn 6.22. The cross-coupled stiffness terms used for the case with the tape on the shaft are shown in Table 8, and the eigenvalue result with the damping ratios is shown in Table 9.

The damping ratios were further verified by plugging in the damping value obtained above as C_{XX} and C_{YY} terms in the XLUSEKCM file, and the eigenvalue case was run as done above

with zero coefficients for the bearings. The same damping ratios were obtained. The damping values used in XLTRC2 is shown in Table 10, and the corresponding damping ratio is shown in Table 11.

Table 8: Cross-coupled stiffness terms to represent the actual damping in the system

XLUseKCM™ **User Defined Support Stiffness, Damping, and Mass Rotordynamic Coefficie**

Title:	Damping Kxy and Kyx values for the freefree case to simulate zeta values

Perform a Paste/Special/Link for the Title box within XLTRC to create a link to your rotor model.

Speed	Kxx	Kxy	Kyx	Kyy	Cxx	Cxy	Cyx	Cyy
rpm	lb/in	lb/in	lb/in	lb/in	lb-s/in	lb-s/in	lb-s/in	lb-s/in
1	0.	-9520.	9520.	0	0	0	0	0
2	0.	-9520.	9520.	0	0	0	0	0
3	0.	-9520.	9520.	0	0	0	0	0
4	0.	-9520.	9520.	0	0	0	0	0

Table 9: Eigenvalue for the free-free case showing the damping ratio

Speed	cpm7	zeta8	cpm8	zeta9	cpm9	zeta10	cpm10	zeta11
1.	985.9	0.703	985.9	-0.005	7903.3	**0.0050957**	**7903.3**	0.000
185.	986.0	-0.005	7902.1	0.005	7904.5	0.000	22603.7	0.000
369.	986.0	-0.005	7900.9	0.005	7905.7	0.000	43014.7	0.000
554.	986.0	-0.005	7899.7	0.005	7906.9	0.000	60221.1	0.000
738.	986.0	-0.005	7898.5	0.005	7908.1	0.000	60270.5	0.000
923.	986.0	-0.005	7897.3	0.005	7909.4	0.000	60320.1	0.000
1108.	986.0	-0.005	7896.1	0.005	7910.6	0.000	60369.9	0.000
1292.	986.0	-0.005	7894.9	0.005	7911.8	0.000	60420.0	0.000
1477.	986.0	-0.005	7893.7	0.005	7913.0	0.000	60470.2	0.000

The value of the damping that matched the damping ratio turned out to be 11.5 lb-s/in. This value was used to create a set of cross-coupled speed dependant bearing stiffness coefficients represented by Eqn 6.22, but replacing the natural frequency with the running speed. The eigenvalues (Table 12) were determined for the case with the bearings and with the effect of the foundation, and the OSI was found to be 4800 rpm. The running tests showed on OSI near 5200 rpm.

Table 10: Damping values used in XLTRC2 to match the damping ratio

XLUseKCM™ **User Defined Support Stiffness, Damping, and Mass Rotordynamic Coefficients** Press Control-F1 for help.

Title: Damping Kxy and Kyx for free free case to simulate the zeta values.

Perform a Paste/Special/Link for the Title box within XLTRC to create a link to your rotor model.

Speed	Kxx	Kxy	Kyx	Kyy	Cxx	Cxy	Cyx	Cyy	Mxx	Mxy	Myx	Myy
rpm	lb/in	lb/in	lb/in	lb/in	lb-s/in	lb-s/in	lb-s/in	lb-s/in	lb-s**2/in	lb-s**2/in	lb-s**2/in	lb-s**2/in
1	0.	0.	0.	0	11.5	0	0	11.5	0	0	0	0
2	0.	0.	0.	0	11.5	0	0	11.5	0	0	0	0
3	0.	0.	0.	0	11.5	0	0	11.5	0	0	0	0
4	0.	0.	0.	0	11.5	0	0	11.5	0	0	0	0

Table 11: Damping ratios obtained from plugging in damping values at the disk-shaft interface

Speed	cpm8	zeta9	cpm9	zeta10	cpm10	zeta11	cpm11	zeta12
1.	9.7	1.000	0.0	0.005	7903.1	**0.0050932**	**7903.1**	0.000
185.	9.7	0.000	16.6	1.000	0.0	0.005	7901.9	0.005
369.	0.0	0.005	7900.7	0.005	7905.5	0.000	22550.2	0.000
554.	0.1	0.000	22496.9	0.000	22818.8	0.001	43000.6	0.001
738.	0.1	0.001	42986.8	0.001	43097.9	0.000	60270.5	0.000
923.	0.1	0.000	60320.1	0.000	59833.5	0.000	101459.9	0.000
1108.	0.1	0.000	60369.9	0.000	59785.9	0.000	102135.9	0.000

Table 12: Eigenvalues for case with tape

Speed	zeta1	cpm1	zeta2	cpm2	zeta3	cpm3
3138.	0.000	9.7	0.039	2690.5	0.060	2863.7
3323.	0.000	9.7	0.038	2702.0	0.061	2852.7
3508.	0.000	9.7	0.036	2716.4	0.063	2838.9
3692.	0.000	9.7	0.033	2733.4	0.066	2822.7
3877.	0.000	9.7	0.027	2749.0	0.072	2807.9
4062.	0.000	9.7	0.021	2759.8	0.078	2798.0
4246.	0.000	9.7	0.014	2767.2	0.084	2791.7
4431.	0.000	9.7	0.008	2772.8	0.090	2787.3
4615.	0.000	9.7	0.003	2777.3	0.096	2784.1
4800.	0.000	9.7	**-0.003**	**2781.3**	0.101	2781.5
4985.	0.000	9.7	-0.008	2784.8	0.106	2779.5
5169.	0.000	9.7	-0.013	2788.1	0.111	2777.8
5354.	0.000	9.7	-0.018	2791.3	0.116	2776.4
5538.	0.000	9.7	-0.023	2794.3	0.121	2775.2

The above tests confirmed that the self-bonding tape increases the internal damping in the system. To further verify the validity of this method, the disk was removed from the shaft and the shaft was shaken both with and without the tape. The previously described method of determining the internal damping in a rotor by conducting free-free shaker tests was used.

Shaker tests of the shaft-only system

The shaft was hung free-free and was shaken as was done for the disk-shaft system.

Modeling the shaft system

Since the shaft is a uniform beam, exciting it with a periodic force will excite all its mode shapes and resulting in an infinite degree of freedom system. But in practice the shaft can be modeled as a two DOF system as was done for the disk-shaft system.

Determination of modal mass

The shape of the first resonant frequency will be a half sine mode shape with the ends of the shaft and the center 180 degrees out of phase. The expression for the modal mass is known in terms of a 2 DOF model, as was shown for the disk-shaft system (Eqn 6.7). The force applied at the center causes the mass at the center m_{cen} to vibrate with a velocity v_{cen} and the ends of the shaft with mass m_{end} with a velocity v_{end}. Applying the law of conservation of momentum to the 2 DOF system model in Figure 45, we get

$$m_{cen}\ v_{cen} + m_{end}\ v_{end} = 0 \qquad \textbf{Eq 6.24}$$

Differentiating Eqn 6.21 we get

$$m_{cen}\ a_{cen} + m_{end}\ a_{end} = 0 \qquad \textbf{Eq 6.25(a)}$$

which implies that

$$\frac{m_{end}}{m_{cen}} = -\frac{a_{cen}}{a_{end}} \qquad \textbf{Eq 6.25(b)}$$

The accelerometers measure the values of a_{cen} and a_{end}. Solving for m_{cen} and m_{end} from equations 6.7 and 6.25 (b), and taking into account the difference in phase between a_{cen} and a_{end} to get rid of the negative sign in Eqn 6.25 (b), we get

$$m_{cen} = \left[\frac{1}{\frac{a_{cen}}{a_{end}}} + 1 \right] M_{eq(sh)} \qquad \textbf{Eq 6. 26}$$

$$m_{end} = \frac{a_{cen}}{a_{end}} m_{cen} \qquad \textbf{Eq 6. 27}$$

An XLTRC2 model was created for the shaft, and the resonant frequency of the free-free modes was correlated with the experimental results. The modal mass of the system was found using Eqn 6.14. Using the modal mass and the ratio of the acceleration at the center to the acceleration at the end, the values of m_{cen} and m_{end} were determined. The modal mass from XLTRC2 was obtained as 13.30 lb.

$$M_{eq(sh)} = 6.05 \text{ kg } (13.03\text{lb})$$

Determination of modal stiffness

As done above, the modal stiffness was determined using Eqn 6.16 and was found to be

$$K_{eq(sh)} = 7.29 \text{ MN/m } (41615.04 \text{ lb/in})$$

Determination of internal damping

The damping was determined using the 90 degree phase shift method and by curve-fitting Eqn 6.12 with the calculated values of modal mass and stiffness to the experimental data and tweaking the damping value until it matched the peak of the experimental data. A set of coefficients was also obtained using the curve-fitting function ‘genfit’ in Mathcad. These two curves were compared with the experimental one.

Results for the shaft system

The data were gathered using LabVIEW and analyzed using Mathcad, as was done for the disk-shaft system. The shaft was hung free-free without any tape and was shaken with the same arrangement as done before. The results are summarized in Table 13. A sample curve fit is shown in Figure 49. The values for damping from the 'genfit' algorithm in Mathcad did not give reasonable results and hence were omitted.

A close look at the spectrum of the force transducer (Figure 50) showed a huge drop in the amplitude at frequencies close to the resonant frequency. The spectrum of the force transducer is an indication of the energy transmitted to the system. The shaker excites all frequencies between 0 and 200 Hz. As the shaking frequency approaches the resonant frequency, the structure starts vibrating with high amplitudes, and very little energy is required to produce a large response. Reference [27] mentions that this effect happens if the settings of the power amplifier are not re-adjusted close to the resonant frequency, to accommodate for the structural influences. As a result, the structure tends to impart an opposing force to the stinger, which reduces the effective force imparted to the structure, whereas the voltage measured by the accelerometer is not actually due to the forcing function, but due to the vibration of the structure itself. The frequency

Table 13 : Modal parameters for shaft with standard stinger

Method used	**Stiffness** **lb/in (N/m)**	**Mass** **lb-s^2/in (kg)**	**Damping** **lb-s/in (N-s/m)**
90-degree damping(average values)	Not Applicable	Not Applicable	0.0696 (12.19)
Curve fit for the theoretical equations	41333.36 (7.24E6)	0.0342 (6.00)	0.0525 (9.20)
Curve fit from the Mathcad algorithm(average)	40983.01 (7.18E6)	0.0339 (5.96)	------

measured by the accelerometer in the above procedure was 173.5 Hz, while the transfer function had a peak at 175 Hz.

Mitchell and Elliot [25] suggest that the stinger used to transmit the forces to the system must be appropriately chosen. The ideal structural analysis would be to excite the structure with a force in one direction and expect a response only in that direction. However, due to the stiffness of the stinger, such an approach could introduce unwanted restraints in the system, causing it not only

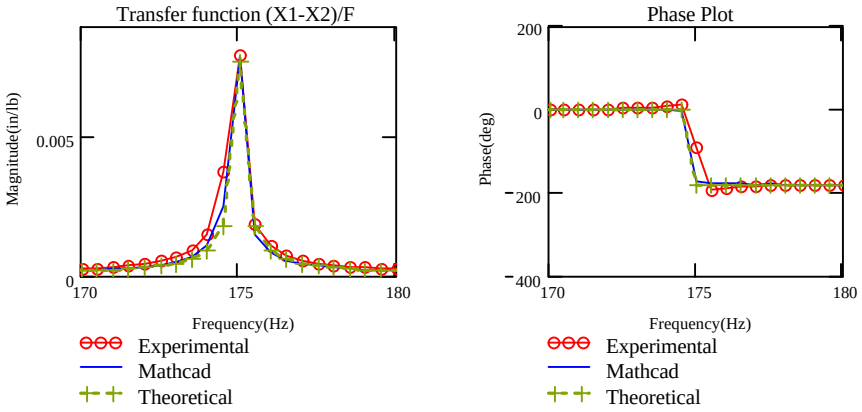

Figure 49: Shaft shaken with the standard stinger

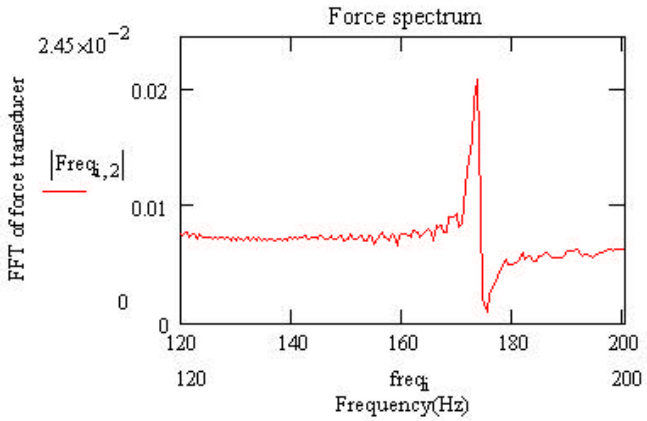

Figure 50 : Spectrum of force transducer

to translate but also to rotate. Hence if the aim were to excite and measure only the linear response due to a forcing function, it would be necessary to allow the stinger to rotate by itself and not impose any restraint on the structure. This requires using a stinger that is stiff in the axial direction (direction of excitation), but flexible along other axes. Reference [26] suggests use of a piano wire for the stinger element. Reference [27] mentions the case of the drop in the force spectrum. They suggest that for systems with light damping, these effects must be taken into account.

Experiments with wire stinger

To study the effect of the stinger on the measurements, a steel wire element was used instead of the standard stinger. The arrangement is shown in Figure 51. To validate the results, a mass calibration [28] was done with an accelerometer and a force transducer. To avoid any effect of the shaker mass, a smaller shaker (manufactured by Wilcoxon) weighing approximately 15 kg (7 lb) was used for the testing. The shaker was hung free-free and was hooked, using the steel wire stinger, through the force transducer on to a small test mass of known weight, which was also

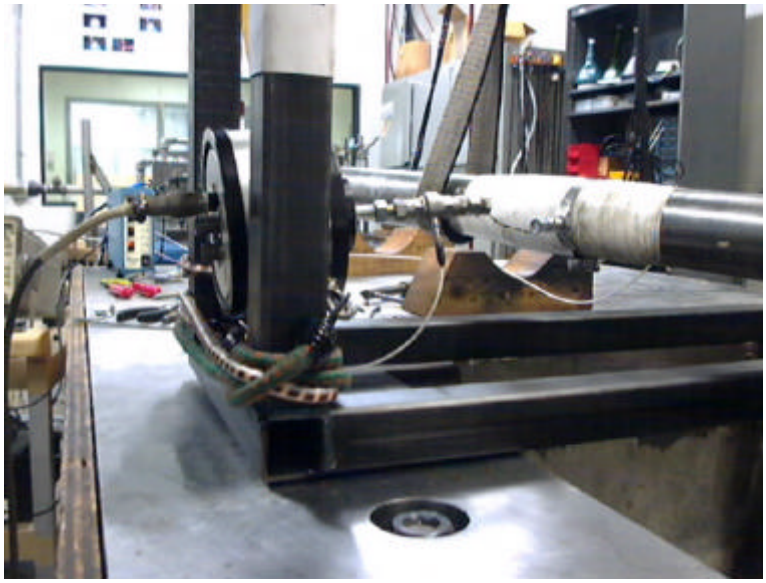

Figure 51: Shaker test with the wire stinger

hung free. An accelerometer was placed on the test mass. Since the applied force causes the mass to vibrate, the transfer function of the acceleration to the applied force applied will be inversely related to the test mass, if the sensitivities of the instrumentation used are correct. The test mass was shaken with a periodic chirp signal from 0 to 200 Hz, and the transfer function of the force to the acceleration was recorded to compute the mass. The mass was computed to be 9.2 kg (4.2 lb), which was same as the value, measured using a weighing machine. The transfer function result is shown in Figure 52. The experiment proves that the calibration constants for the measurement devices are correct. Though the spectrum does not look good at low frequencies, the constancy of the curve at frequencies close to the resonant frequency gives confidence in using the wire stinger for further testing. Tests were done both with and without the tape on the shaft, and the results are summarized below in Table 14.

A look at the frequency spectrum of the force transducer with the steel wire stinger is shown in Figure 53. No dip is noted close to the resonant frequency (175 Hz). Further, both the accelerometer response peak and the peak of the transfer function are at the same frequency (175 Hz). The same technique was used for the disk-shaft system, and the results are summarized in Table 15.

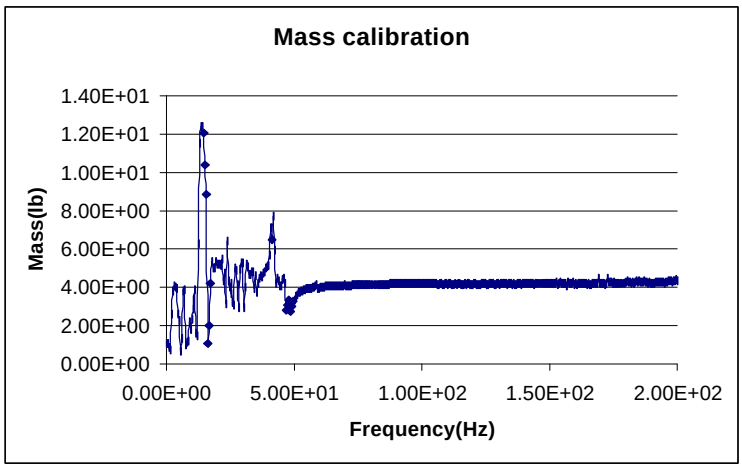

Figure 52: Mass calibration curve

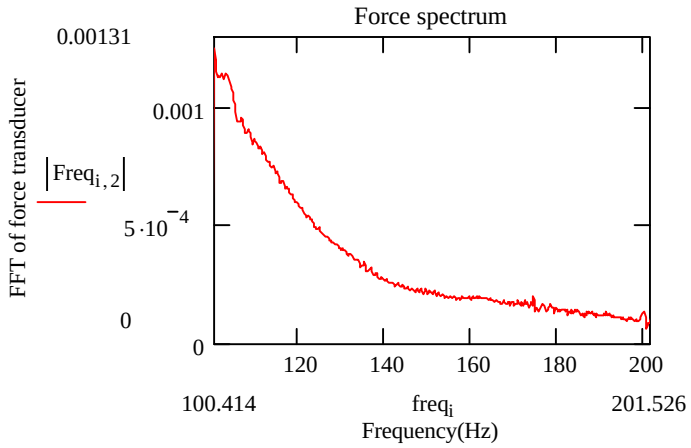

Figure 53 : Spectrum of force transducer with wire stinger

Table 14 : Modal parameters for shaft with wire stinger

Description	Method used	Stiffness lb/in (N/m)	Mass lb-s^2/in (kg)	Damping lb-s/in (N/m)
Without tape	90-degree damping (average values)	NA	NA	0.0579 (10.16)
	Curve fit for the theoretical equations	41333.44 (7.24E6)	0.0341 (6.00)	0.0542 (9.50)
	Curve fit from the Mathcad algorithm(average)	33021.79 (5.79E6)	0.0274 (4.81)	0.0525 (9.20)
With tape	90-degree damping(average values)	NA	NA	0.0593 (10.38)
	Curve fit for the theoretical equations	41215.43 (7.22E6)	0.0341 (6.00)	0.0550 (9.64)
	Curve fit from the Mathcad algorithm(average)	27831.59 (4.88E6)	0.0230 (4.05)	0.0522 (9.14)

Table 15 : Modal parameters for disk-shaft with wire stinger

	Method used	Stiffness lb/in (N/m)		Mass lb-s^2/in (kg)		Damping lb-s/in (N-s/m)	
	Type of fit	**Loose**	**Tight**	**Loose**	**Tight**	**Loose**	**Tight**
Without tape	90-degree damping (average)	NA	NA	NA	NA	0.2519 (44.14)	0.1804 (31.62)
	Curve fit for theoretical equations	26817.97 (4.69E6)	27462.87 (4.81E6)	0.04313 (7.57)	0.04313 (7.57)	0.2519 (44.14)	0.1804 (31.62)
	Curve fit From Mathcad algorithm (average)	25574.84 (4.48E6)	20741.01 (3.63E6)	0.04121 (7.24)	0.0322 (5.66)	0.2316 (40.59)	0.1512 (26.50)
With tape	90-degree damping (average)	NA	NA	NA	NA	0.2132 (37.39)	0.1754 (30.58)
	Curve fit for theoretical equations	26817.97 (4.69E6)	27462.87 (4.81E6)	0.04313 (7.57)	0.04313 (7.57)	0.2132 (37.39)	0.1754 (30.58)
	Curve fit From Mathcad (average)	22057.03 (3.86E6)	21584.86 (3.78E6)	0.0373 (6.05)	0.0339 (5.96)	0.2030 (35.57)	0.1671 (29.98)

Table 16 : Comparison of tests done with the two types of stingers for the disk-shaft system

	Method used	Damping lb-s/in (N-s/m)
Without Tape	**Standard Stinger**	0.2319 (40.64)
	Wire stinger	0.2519 (44.14)
With Tape	**Standard Stinger**	0.3204 (56.15)
	Wire stinger	0.2132 (37.39)

Discussion of shaker test results

An attempt has been made to quantify internal friction by conducting shaker tests both on the disk-shaft system and on the shaft. The internal damping was increased by adding a self-bonding tape on the shaft. Tests were done both by hanging the shaker and by fixing it on a table. Tests were also done with the standard metal stinger and with the wire stinger, and the results are compared in Table 16.

The project depicts a method of determining the internal damping in the system by conducting shaker tests. Table 1 shows that the addition of the tape increases the internal damping in the system, and hence gives rise to the subsynchronous frequencies during the running tests, irrespective of the fit. However, it can be observed that the magnitude of the subsynchronous is lower in the case of the tight fit, which proves that with the loose fit, the damping effect due to the fit between the sleeve and the disk also comes into action in addition to the damping due to the tape.

The experiments with the wire stinger do not give results that match with the predicted values of equivalent stiffness and mass. The reason for this is not known.

The comparison of the results in Table 16 show that the measured value of the internal damping does not change much for the case without the tape, regardless of the type of stinger used. However, the incompatible tests with the tape are presented since the literature suggests the use of a flexible stinger to avoid moments and back-forces from the shaker to the structure. The fact that the experimental data for the standard stinger match the equivalent modal mass and stiffness obtained from using the XLTRC2 model and free-free rap tests gives confidence in believing those damping values. The signal conditioner for the accelerometers and the force transducer have a built-in filter for AC biasing, thus avoiding any possible DC offset into the signal that goes to LabVIEW. The validity of using an accelerometer to get the displacements by dividing by the square of the frequency was checked by performing a similar experiment on another test rig that was cantilevered; measurements with the displacements from the accelerometer and a proximity probe were compared. The measurements from the two tests agreed with each other.

CHAPTER VII

SUMMARY AND FUTURE SCOPE

Having investigated experimental methods of determining internal damping in a system, the principal experimenter next proposes to try differentiating between benign and potentially harmful vibrations. The measurement of non-destructive subsynchronous vibrations shows that even though an “instability” is detected, there may be no reason for shutdown of machinery. Tape was used to create internal friction. However, the practical industry case is assembly interface that causes the internal friction. Many turbomachines have shrink-fit aluminum wheels that may be potential sources of instability. To mimic this situation, an aluminum sleeve could be shrunk fit on the shaft and the shaker and running tests could be conducted. If this system goes unstable, the filtered orbit of the subsynchronous vibration can be compared with the filtered orbit for the subsynchronous vibration in other cases, and conclusions can be made based on the shape of the orbits.

The advantage of probing into the shape of the filtered subsynchronous orbit is that one might be able to use this for real-time machinery diagnostics, and rather than blindly shutting down a machine on seeing a subsynchronous component, one might want to analyze it first before coming to a decision.

From a design point of view, one should bear in mind the possibility of instabilities due to built-up rotors. Once a rotor is designed and a prototype made, it could be hung free-free and shaken to determine the internal damping as described above. These results could be incorporated into a computer simulation to determine if the system will go unstable.

REFERENCES

[1] Jeffcott, H.H., 1919, “The Lateral Vibrations of Loaded Shafts in the Neighbourhood of a Whirling Speed: The Effect of Want of Unbalance”, Philosophical Magazine, Series 6, **37**, pp. 304-318.

[2] Newkirk, B.L., 1925, “Measurement of Internal Friction in a Revolving Deflected Shaft”, General Electric Review, **28**, pp. 554-558.

[3] Kimball, A.L. Jr., 1924, “Internal Friction Theory of Shaft Whirling”, General Electric Review, **27**, pp. 244-251.

[4] Ehrich, F.F., 1964, “Shaft Whirl Induced by Rotor Internal Damping”, Journal of Applied Mechanics, **31**, pp. 279-282.

[5] Gunter, E.J., 1967, “The Influence of Internal Friction on the Stability of High Speed Rotors”, Journal of Engineering for Industry, (November), **8**, pp. 683-688.

[6] Gunter, E.J. Jr., Trumpler, P.R., 1969, “The Influence of Internal Friction on the Stability of High Speed Rotors with Anisotropic Supports”, Journal of Engineering for Industry, (November), pp. 1105-1113.

[7] Begg, I.C., “Friction Induced Rotor Whirl – A Study in Stability”, ASME 73-DET -106.

[8] Vance, J.M, Lee, J, 1973, “Stability of High Speed Rotors with Internal Friction”, ASME Publication, ASME Paper No. 73-DET-127.

[9] Black, H.F., 1976, “The Stabilizing Capacity of Bearings for Flexible Rotors with Hysteresis”, Journal of Engineering for Industry, (February), pp. 87-91.

[10] Ying, D., Vance, J.M., 1993, “Effect of Press Fits on Threshold Speeds of Rotordynamic Instability”, TRC Report.

[11] Bently, D.E., Muzsynska, A., 1982, “Rotor Internal Friction Instability”, NASA Conference Publication, Instability in Rotating Machinery, NAS 1-55-2409, pp. 337-348.

[12] Lund, J.W., 1986, “Destabilization of Rotors from Friction in Internal Joints with Micro-slip”, Proceedings of the International Conference on Rotordynamics, pp. 487-491, Tokyo.

[13] Parker, J.S., 1997, “The Development of an Experimental Procedure to Determine the Amount of Active Internal Damping in a Rotor-Bearing System”, M.S. Thesis, Texas A&M University.

[14] Bently, D.E., 1972, "The Re-Excitation of Balance Response Regions by Internal Friction: Kimball Revisited", ASME Paper No. 72-Pet-49.

[15] Albaz.K., 2000, "Effect of Shrink Fits on Threshold Speeds of Rotordynamic Instability", M.S. Thesis, Texas A&M University, December.

[16] Mir.M., 2001, "Effect of Shrink Fits on Threshold Speeds of Rotordynamic Instability", M.S. Thesis, Texas A&M University, December.

[17] Steidel, R.F. Jr., 1988, *An Introduction to Mechanical Vibrations*, John Wiley and Sons, New York, 3rd edition.

[18] Shaw, J., Shaw, S.W., 1989, "Instabilities and Bifurcation in a Rotating Shaft", Journal of Sound and Vibration, **132**, pp 227-244.

[19] Ferrara, P.L., 1977, "Vibrations in a Very High pressure Centrifugal Compressor", ASME Paper No. 77-DET-15.

[20] Gunter, E.J., Kirk, R.G., 1975, "Stability and Transient Motion of a Plain Journal Mounted in Flexible Damped Supports", ASME Paper No. 75-DET-116.

[21] Murphy, B.T., 1984, "Eigenvalues of Rotating Machinery", Ph.D. Dissertation, Texas A&M University, May.

[22] Xu, J., "Rotor Foundation Dynamics for Improved Prediction of Critical Speeds", report (available from Dr. John Vance, Texas A&M University), April 1998.

[23] Lin, Y.Q., 1993, "Rotor Instability Induced by Radial Clearance in Ball Bearing Supports", ASME Paper No. 93-GT-29.

[24] Vance, J.M., 1988, *Rotordynamics of Turbomachinery*, John Wiley and Sons, New York.

[25] Mitchell, L.D., Elliott K.B., 1984, "How to Design Stingers for vibration Testing of Structures", Sound and Vibration, (April), **18**, pp. 14-18.

[26] Maia, N.M.M, Silva, J.M.M et al, 1997, *Theoretical and Experimental Modal Analysis*, John Wiley and Sons, New York.

[27] Mitchell, L.D., Mitchell, L.D., 1985, "Wrong with Confidence, Analyzer Problems", Proceedings of the 1985 ASME fall Conference on Experimental Mechanics, pp. 120-128.

[28] Ewins D.J., 1984, *Modal Testing, Theory and Practice*, John Wiley and Sons, New York.

APPENDIX A

XLTRC2 Input sheet

The following sheet gives the input values that were supplied to XLTRC2. The dimensions of the shaft, the material and the number of elements are specified

Shaft Properties

Shaft	Starting X_0	Starting Y_0	Int. Hyst. Damping Coeff	Int. Visc. Damping Coeff	Type of Shaft Rotation	Rotation Value	Whirl ======= Spin
#	inches	inches	η_H	η_V	Const or Ratio	rpm or N	ω / Ω
1	0	0	0	0	Ratio	1	1
2	3	0	0	0	constant	0	0
3	45	0	0	0	constant	0	0

Material Properties

Material	Shear Const	Axial Force Const	Density ρ	Elastic Modulus E	Shear Modulus G
#	(sc or -1)	(ax or 0)	lbm/in^3	lbf/in^2	lbf/in^2
1	-1	0	0.283	30.0E+6	12.0E+6
2	-1	0	0.283	30.0E+3	30.0E+3
3	-1	0	0.00001	30.0E+6	12.0E+6

Rotor Model Data Entry: Multiple Shafts, Elements, Sub-Elements and Layers.

Shaft	Element	Sub-Element	Layer	Length	Left		Right		Material	Shear Interact.	Axial Force
					OD	ID	OD	ID			
#	#	#	#	inches	inches	inches	inches	inches	#	(0 or 1)	lbf
1	1	1	1	1.75	2.5	0	2.5	0	1	1	0
1	2	1	1	1.75	2.5	0	2.5	0	1	1	0
1	3	1	1	2.3125	2.5	0	2.5	0	1	1	0
1	4	1	1	2.3125	2.5	0	2.5	0	1	1	0
1	5	1	1	2.3125	2.5	0	2.5	0	1	1	0
1	6	1	1	2.3125	2.5	0	2.5	0	1	1	0
1	7	1	1	2.3125	2.5	0	2.5	0	1	1	0
1	8	1	1	2.3125	2.5	0	2.5	0	1	1	0
1	9	1	1	2.3125	2.5	0	2.5	0	1	1	0
1	10	1	1	2.3125	2.5	0	2.5	0	1	1	0
1	11	1	1	2.5	10	2.5	10	2.5	2	1	0
1	11	1	2	2.5	2.5	0	2.5	0	1	1	0
1	12	1	1	2.5	10	2.5	10	2.5	2	1	0
1	12	1	2	2.5	2.5	0	2.5	0	1	1	0
1	13	1	1	2.3125	2.5	0	2.5	0	1	1	0
1	14	1	1	2.3125	2.5	0	2.5	0	1	1	0
1	15	1	1	2.3125	2.5	0	2.5	0	1	1	0
1	16	1	1	2.3125	2.5	0	2.5	0	1	1	0
1	17	1	1	2.3125	2.5	0	2.5	0	1	1	0
1	18	1	1	2.3125	2.5	0	2.5	0	1	1	0
1	19	1	1	2.3125	2.5	0	2.5	0	1	1	0
1	20	1	1	2.3125	2.5	0	2.5	0	1	1	0
1	21	1	1	2.375	2.5	0	2.5	0	1	1	0
1	22	1	1	2.375	2.5	0	2.5	0	1	1	0
1	23	1	1	2	1	0	1	0	1	1	0
2	1	1	1	0.5	4.5	3.5	4.5	3.5	3	1	0
2	2	1	1	0.5	4.5	3.5	4.5	3.5	3	1	0
3	1	1	1	0.5	4.5	3.5	4.5	3.5	3	1	0
3	2	1	1	0.5	4.5	3.5	4.5	3.5	3	1	0

Station Numbers

Left Station	Right Station
#	#
1	2
2	3
3	4
4	5
5	6
6	7
7	8
8	9
9	10
10	11
11	layer
layer	12
12	layer
layer	13
13	14
14	15
15	16
16	17
17	18
18	19
19	20
20	21
21	22
22	23
23	24
25	26
26	27
28	29
29	30

APPENDIX B

Uncertainty analysis

The uncertainty in the experiments comes from the measurement devices, which are the accelerometer, proximity probes, force transducer, ADRE and the signal analyzer. The uncertainties in the analyzer and in ADRE depend on the bandwidth of the measured data that is specified. The manufacturer's specifications for these devices are as follows:

Proximity probes	Accuracy ± 5%
Force transducer	Accuracy ± 1 %
ADRE	Bandwidth 20 rpm
Signal analyzer	Bandwidth 0.5 Hz
Accelerometer	Accuracy ± 5%

An uncertainty also arises in the curve fit that is done in Mathcad. The curve fit is valid only for the bandwidth specified by the analyzer.

The deviation of the readings was computed using the standard deviation formula

$$SD = \sqrt{\frac{\sum (x_{mean} - x_i)^2}{N}}$$

where x_{mean} is the average of the samples, $\{x_i\}$ is each of the samples whose mean is taken, and N is the number of samples. Using this formula the standard deviation for one set of readings was obtained as 0.00263. The same method was used for all the samples.

The Kline-McClintock rule for uncertainty is given by the equation

$$U_R = \sqrt{\left(\frac{\partial R}{\partial x1} U_1\right)^2 + \left(\frac{\partial R}{\partial x2} U_2\right)^2 + \ldots + \left(\frac{\partial R}{\partial xn} U_n\right)^2} \qquad \textbf{Eq. AC 1}$$

where the uncertainty measure U_R is the equation that is a function of the individual uncertainties, U_1, U_2,…, U_n based on the accuracy of the individual measurements. To measure the damping in the system, an accelerometer and a force transducer are used, and the transfer function of the ratio of the acceleration to the force is determined. Hence

$$U(a,F) = \frac{a}{F}$$

Using Eqn AC1 for this transfer function, the equation for the uncertainty is

$$U_R = \sqrt{\left(\frac{U_a}{F}\right)^2 + \left(\frac{aU_f}{F^2}\right)^2}$$

where $U_a = 0.05 \times a$, $U_f = 0.01 \times F$, as obtained from the accuracy values of the instruments from the specifications. Substituting these values we get

$$\frac{U_R}{\frac{a}{F}} = 5.099\%$$

APPENDIX C

Determination of cross-coupled stiffness terms that represent the destabilizing force

The destabilizing force produced by the internal friction damping, which is hysteretic, can be modeled as cross-coupled coefficients [24],[5], represented by $K_{XY} = -K_{YX} = c_i\, w$ where c_i is the internal damping coefficient, K_{XY} and K_{YX} are the cross-coupled coefficients. The resultant force due to internal friction is stabilizing at speeds below the critical speed and destabilizing at speeds above the critical. The forces produced by the cross-coupled stiffness terms are shown in Figure 60, where $Fx = -K_{XY} Y$, $Fy = K_{YX} X$, Fr is the resultant force. To satisfy this condition, the cross-coupled coefficients are chosen in such a way that $K_{XY} < 0$, $K_{YX} > 0$ below the critical, and $K_{XY} > 0$, $K_{YX} < 0$ above the critical speed.

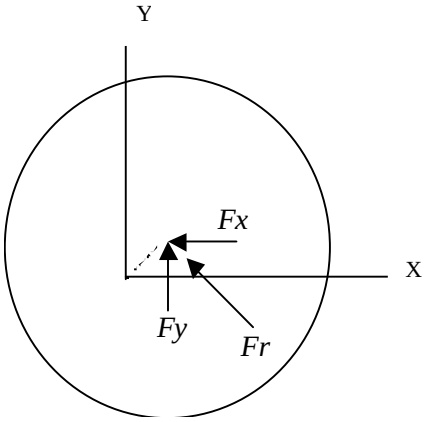

Figure 54: Cross-coupled stiffness representing a destabilizing force

APPENDIX D

Figures in SI units

Appendix D gives the transfer function magnitude-phase results and the comparison of the damping values of the shaker tests in SI units.

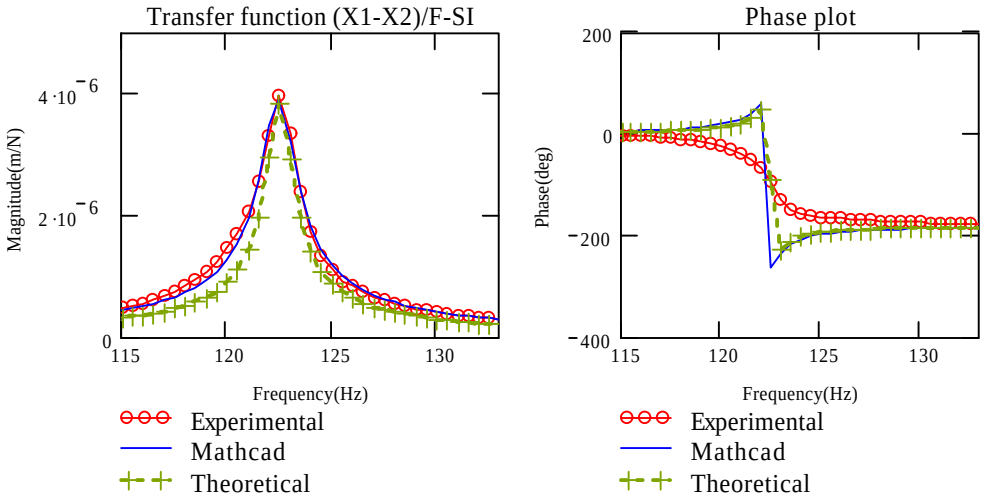

Figure AC 1: Loose fit with tape on both sides (SI units)

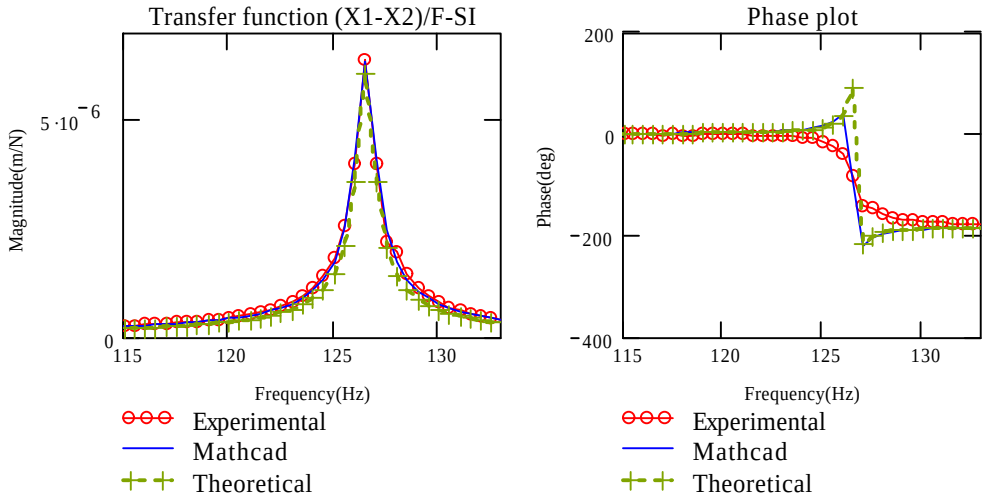

Figure AC 2: Tight fit with tape on both sides (SI units)

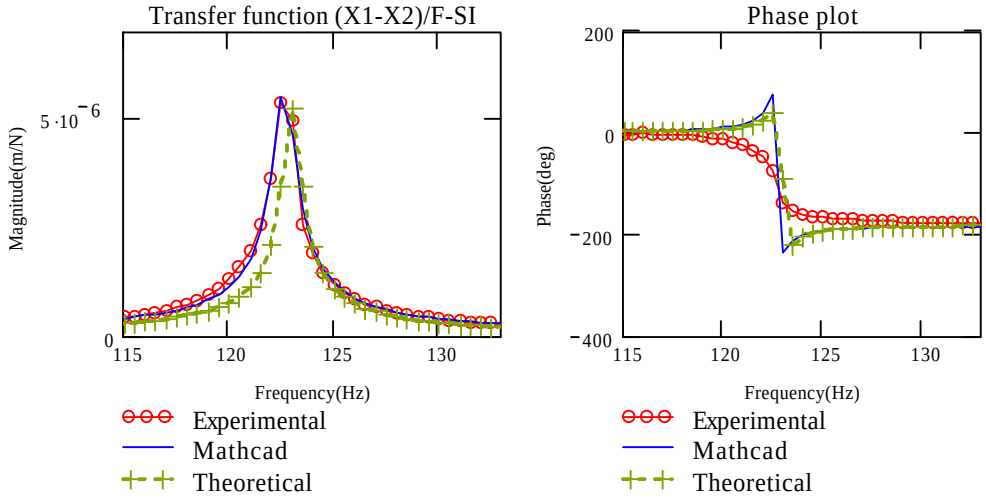

Figure AC 3: Loose fit with no tape (SI units)

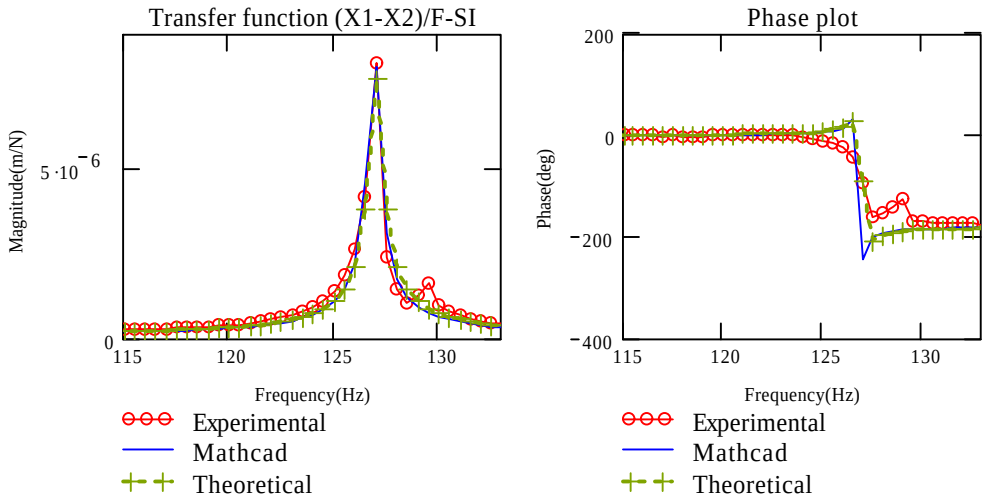

Figure AC 4: Tight fit with no tape (SI units)

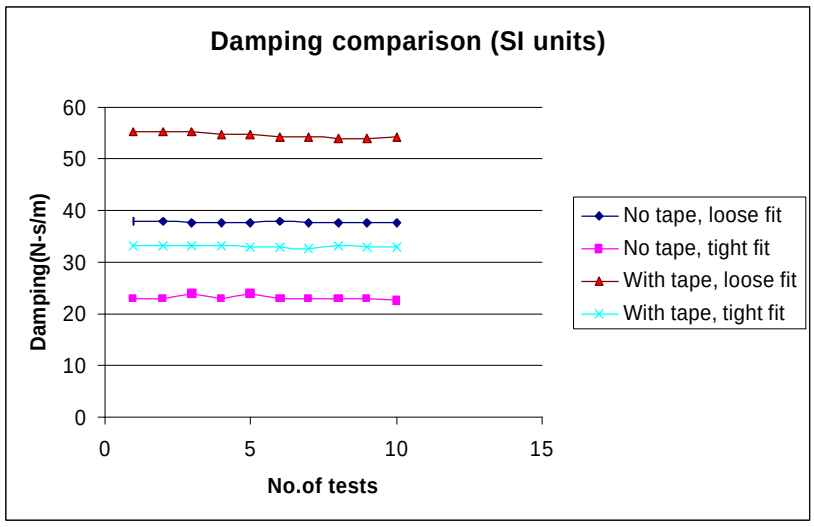

Figure AC 5: Comparison of damping values for the disk-shaft system with standard stinger (SI units)

VITA

ANAND SRINIVASAN
Plot 58, Door 5/2, Rajaram Salai, K.K.Nagar, Trichy 620021, INDIA.
Ph: 91-431-2459293; anand_s78@yahoo.com

EDUCATION

Texas A&M University, College Station, TX — Sep *2000 – May 2003*
Master of Science in Mechanical Engineering, — Degree GPA: 3.5/4.0

University of Madras, Chennai, India — *Aug 1996 - May 2000*
Bachelor of Engineering, Mechanical Engineering — Overall GPA 3.96/4.00

EXPERIENCE

Research Assistant, Turbomachinery Laboratory, Texas A&M University
Sep 2000 – May 2003

- Working under Prof. **John Vance**, involved in experimental static (determination of rotordynamic coefficients – stiffness, mass, damping) and dynamic analyses (response of machinery to excitation forces – collection and interpretation of Bode, Waterfall plots) of test rigs.
- Was involved in the hardware construction (piping for lube lines, foundation, electrical supplies) and commissioning of the General Electric 7HDL Turbocharger for testing purpose.

Lucas TVS, Chennai, India May 1997

Underwent an Internship in the maintenance department in this leading automotive starter manufacturing company and learned various skills concerning manufacturing processes.

COMPUTER SKILLS

- Worked with programming languages such as BASIC, FORTRAN90, C, Excel Visual Basic
- Proficient in SolidWorks, a Solid Modeling package and COSMOS, a finite element analysis package; Experience in Pro Engineer 2000i and Auto CAD
- Knowledge of XLTRC, an Excel based modeling software for rotating machinery and ADRE, a data acquisition system
- Fluent usage of packages such as MS Word, MS Excel, MS PowerPoint, MS FrontPage, Adobe Photoshop
- Experience in Maple, MATLAB, MathCAD, LABVIEW
- Knowledge of Cambridge Engineering Selector, a material and process selection tool